

Mechanics and Modeling of Cold Rolling of Polymeric Films at Large Strains - A Rate-Independent Approach

Nikhil Padhye

Contents

1	Introduction	7
2	Mechanics and Modeling of Cold Roll-Bonding of Solid-State Polymeric Films	11
2.1	Materials	11
2.2	Estimates based on rigid perfectly-plastic material model	13
3	Finite Strain Rate-Independent Elastic-Plastic Material Model for Polymeric Films	16
3.1	Rate-Independent Deformation Model Based on Multiplicative Decomposition of Deformation Gradient	18
3.1.1	Principal of virtual power	19
3.1.2	Consequences of frame indifference	20
3.1.3	Macroscopic force balance	21
3.1.4	Microscopic force balance	22
3.1.5	Rate-independent elastic-plastic constitutive response	23
3.1.6	Plastic flow: yield and consistency condition	26
3.1.7	Time Integration for Rate-Independent Multiplicative Plasticity	28
3.2	Hypoelasticity: Additive Decomposition of Spatial Strain Rate	33
3.2.1	Time Integration Rate-Independent Hypoelasticity	36
3.3	Solution to Global Equilibrium Equations Using Abaqus Explicit Dynamics	38
3.4	Contact Interaction and Friction	39
4	Experimental and Simulation Results	39

5	Equivalency between hypoelasticity and multiplicative decomposition of deformation gradient formulations	45
6	Conclusions	47
7	Acknowledgments	48

Abstract

Recently, a new phenomenon of bonding polymeric films in solid-state, via symmetric rolling, at ambient temperatures ($\approx 20^\circ\text{C}$) well below the glass transition temperature ($T_g \approx 78^\circ\text{C}$) of the polymer, has been reported. In this new type of bonding, polymer films are subject to plane strain active bulk plastic compression between the rollers during deformation. Here, we analyze these plane strain cold rolling processes, at large strains but slow strain rates, by finite element modeling. We find that at low temperatures, slow strain rates, and moderate thickness reductions during rolling (at which Bauschinger effect can be neglected for the particular class of polymeric films studied here), the task of material modeling is greatly simplified, and enables us to deploy a computationally efficient, yet accurate, finite deformation rate-independent elastic-plastic material behavior (with inclusion of isotropic-hardening) for analyzing these rolling processes. The finite deformation elastic-plastic material behavior based on (i) the additive decomposition of stretching tensor ($\mathbf{D} = \mathbf{D}^e + \mathbf{D}^p$, i.e., a hypoelastic formulation) with incrementally objective time integration and, (ii) multiplicative decomposition of deformation gradient ($\mathbf{F} = \mathbf{F}^e \mathbf{F}^p$) into elastic and plastic parts, are programmed and carried out for cold rolling within Abaqus Explicit. Frictional interactions are modeled using a consistent rate-independent Coulombic law. Predictions from both the formulations, i.e., hypoelastic and multiplicative decomposition, exhibit a close match with the experimentally observed rolling loads. We find that no specialized hyperelastic/visco-plastic material model is required to describe the behavior of the particular blend of polymeric films, under the conditions described here, thereby significantly speeding up the computation for steady-state rolling simulations. It is revealed that under the deformation conditions when principal axes show negligible rotation, hypoelastic formulation is valid at large elastic stretches. Moreover, the use of classical rigid-plastic modeling (which is often applicable to metals) is found to greatly underestimate the rolling loads for polymers, due to large elastic stretches in the polymer films at large strains. Deformation aspects of solid-state polymeric sheets presented here are expected to facilitate the development of new processes involving (or related to) cold roll-bonding of polymers.

Keywords: plane strain rolling, elasto-plastic analysis, polymer behavior.

Notation

a half contact width in rolling;

da differential area in current configuration;

B reference body;

\mathbf{b}_0 body force (per unit volume) in current configuration;

\mathbf{b} body force (per unit volume) in current configuration with inertia effect included;

c dilatational wave speed;

\mathbf{C}^e elastic right Cauchy–Green strain;
 \mathbb{C} Fourth order elasticity tensor;
 \mathbb{C}^{ep} Elasto-plastic tangent modulus for hypoelasticity;
 $2d$ total compression in the film-stack;
 dv differential volume in current configuration;
 dv^* differential volume of current configuration with respect to a rotated frame;
 dv_R differential volume in the reference configuration;
 \mathbf{D} stretching-rate tensor, symmetric part of velocity gradient \mathbf{L} ;
 \mathbf{D}^e elastic stretching-rate tensor, symmetric part of \mathbf{L}^e ;
 \mathbf{D}^p plastic stretching-rate tensor, symmetric part of \mathbf{L}^p ;
 $\bar{\mathbf{D}}^p$ plastic stretching-rate tensor in current configuration for hypoelasticity;
 E Young’s modulus;
 E_{roller} Young’s modulus of roller;
 E_{film} Young’s modulus of polymer film;
 \mathbf{E}^e Hencky strain given by $\ln(\mathbf{U}^e)$;
 E_e^i eigen values of Hencky strain given by $\ln(\lambda_i^e)$ with $i = 1, 2, 3$;
 $\Delta \mathbf{E}$ spatial incremental strain in hypoelastic formulation;
 $\Delta \mathbf{E}^e$ spatial incremental elastic strain in hypoelastic formulation;
 $\Delta \mathbf{E}^p$ spatial incremental plastic strain in hypoelastic formulation;
 E_{roller} Young’s modulus of the rollers;
 $\Delta \bar{\varepsilon}^{pl}$ incremental equivalent plastic strain;
 $\bar{\varepsilon}^{pl}$ equivalent plastic strain;
 e^p accumulated plastic strain;
 f yield function for multiplicative plasticity;
 f_h yield function for hypoelasticity;
 \mathcal{F} vector of external nodal point forces for the finite element model;
 \mathbf{F} deformation gradient;
 \mathbf{F}^e elastic part of deformation gradient;
 \mathbf{F}^p plastic part of deformation gradient;
 $F_{friction}$ measured force during measurement of coefficient of friction;
 G elastic shear modulus;
 h_1 thickness of film-stack at the inlet;
 h_o thickness of film-stack at the outlet;
 \bar{h} average of the inlet and outlet thicknesses (h_1, h_o);
 h thickness of film-stack (at x coordinate) in the roller bite;

H hardening modulus;
 \mathbf{I} second order identity tensor ;
 \mathbb{I} fourth order identity tensor;
 \mathcal{J} vector of internal nodal point forces for finite element model;
 J determinant of the deformation gradient \mathbf{F} ;
 J^e determinant of deformation gradient \mathbf{F}^e ;
 J^p determinant of deformation gradient \mathbf{F}^p ;
 k yield strength in shear;
 K elastic bulk modulus;
 l_e smallest element dimension in finite element mesh;
 L total load in rolling;
 \mathbf{L} spatial velocity gradient;
 \mathbf{L}^e elastic part of velocity gradient;
 \mathbf{L}^p plastic part of velocity gradient;
 $\tilde{\mathbf{L}}^e$ virtual elastic velocity gradient;
 $\tilde{\mathbf{L}}^p$ virtual plastic velocity gradient;
 $m'g$ weight of the steel block used in friction measurement experiment;
 m velocity-dependent friction factor in range between 0 and 1;
 M moment per-unit width during rolling;
 \mathbf{M}^e Mandell stress, work conjugate to \mathbf{L}^p ;
 \mathcal{M} diagonal lumped mass matrix for global finite elements;
 \mathbf{n} unit vector \mathbf{n} in the deformed configuration;
 \mathbf{N}^p direction of plastic flow (determining \mathbf{D}^p);
 $\bar{\mathbf{N}}^p$ direction of plastic flow transformed into the current configuration (determining $\bar{\mathbf{D}}^p$);
 P material region in the reference configuration;
 P_t material region in the current configuration;
 P_l line loading in rolling;
 \mathbf{Q} frame-rotation;
 \mathbf{r}_i^e orthonormal eigen-vectors of \mathbf{C}^e and \mathbf{U}^e with $i = 1, 2, 3$;
 R radius of rollers;
 \mathbf{R} rotation tensor obtained by the decomposition $\mathbf{F} = \mathbf{R}\mathbf{U}$;
 \mathbf{R}^e rotation tensor obtained by the decomposition $\mathbf{F}^e = \mathbf{R}^e \mathbf{U}^e$;
 \mathbf{R}^p rotation tensor obtained by the decomposition $\mathbf{F}^p = \mathbf{R}^p \mathbf{U}^p$;
 \mathbf{S}^e microstress that is work conjugate to elastic velocity gradient \mathbf{L}^e ;
 \mathbf{T} Cauchy stress;

\mathbf{T}^p microstress that is work conjugate to plastic velocity gradient \mathbf{L}^p ;
 T_g Glass transition temperature;
 $\mathbf{t}(\mathbf{n})$ Traction field (associated with \mathbf{n});
 \mathbf{T}^J Jaumman rate of Cauchy stress;
 \mathbf{U} symmetric and positive-definite stretch tensor from right polar decomposition of \mathbf{F} ;
 \mathbf{U}^e symmetric and positive-definite right elastic stretch tensor from right polar decomposition of \mathbf{F}^e ;
 \mathbf{U}^p symmetric and positive-definite right plastic stretch tensor from right polar decomposition of \mathbf{F}^p ;
 $\dot{\mathcal{U}}$ vector of nodal point velocities for the finite element model;
 v_o exit speed of the film-stack;
 \mathbf{v} spatial velocity;
 $\tilde{\mathbf{v}}$ virtual spatial velocity;
 v_x velocity at any section (at a distance of x units from the exit);
 \mathbf{V} symmetric and positive-definite stretch tensor from left polar decomposition of \mathbf{F} ;
 \mathbf{V}^e symmetric and positive-definite elastic stretch tensor from left polar decomposition of \mathbf{F}^e ;
 \mathbf{V}^p symmetric and positive-definite plastic stretch tensor from left polar decomposition of \mathbf{F}^p ;
 \mathcal{V} set of virtual velocity fields;
 \mathbf{W} continuum spin, the anti-symmetric part of \mathbf{L} ;
 \mathbf{W}^e elastic spin, the anti-symmetric part of \mathbf{L}^e ;
 \mathbf{W}^p plastic spin, the anti-symmetric part of \mathbf{L}^p ;
 x, y, z coordinate variables;
 \mathbf{x} position of a material point in current configuration;
 \mathbf{X} position of a material of a body in reference configuration;
 Y scalar yield-strength and radius of the spherical yield strength;
 Y' hardening modulus;
 τ_{shear} tangential traction due to friction;
 σ_v equivalent (von Mises) stress;
 $\sigma_{y, film}$ yield-strength of film;
 \mathcal{U} Nodal point displacements in the finite element solution;
 ν Poisson's ratio;
 τ duration of contact in rollers during rolling;
 μ coefficient of friction;
 $(\dot{})$ time rate of a quantity;
 $|()|$ norm of the quantity;
 $(\ddot{})$ double derivative w.r.t. time;
 $\mathbf{A} : \mathbf{B}$ inner product of two second order tensors \mathbf{A} and \mathbf{B} ;

$\text{Sym} ()$ symmetric part of the operand;
 ∇ gradient with respect to material coordinates \mathbf{X} ;
 $()^{-1}$ inverse of the tensor operand;
 $()^{\top}$ transpose of the tensor operand;
 $\det ()$ determinant of the tensor operand;
 $\text{tr} ()$ trace of the tensor operand;
 $\text{grad} ()$ gradient of the quantity with respect to spatial coordinates \mathbf{x} ;
 $()^*$ transformed quantity in rotated-frame;
 $\text{div} ()$ divergence of the quantity with respect to spatial coordinates \mathbf{x} ;
 $()_0$ deviatoric part of the tensor quantity;
 ν Poisson's ratio;
 χ deformation, mapping a material point to a spatial point;
 ρ density at a material point in current configuration ;
 $\mathcal{W}(P_t)$ external power delivered to a body part P_t in current configuration;
 $\mathcal{J}(P_t)$ internal power expended inside a body part P_t in current configuration;
 \mathcal{W}_{int} Virtual internal power;
 \mathcal{W}_{ext} Virtual external power;
 φ free energy per-unit intermediate volume;
 $\tilde{\varphi}$ free energy function expressed in terms of invariants of \mathbf{C}^e ;
 $\hat{\psi}$ free energy function expressed in terms of invariants of \mathbf{U}^e ;
 δ dissipation per-unit intermediate volume;
 Ω frame-spin;
 λ consistency parameter for the yield condition;
 $\dot{\lambda}$ equivalent plastic strain rate;
 λ_i^e positive eigen values of \mathbf{U}^e with $i = 1, 2, 3$;
 ω_i^e positive eigen values of \mathbf{C}^e with $i = 1, 2, 3$;
 ω angular speed of the rollers.

1 Introduction

Several methods, usually referred to as *calendering*, are in practice for processing flat sheet-like materials such as paper, polymers, metals, blankets, cardboard laminates, etc. The central idea in calendering (or alike) methods is to subject the incoming stock of material under compression through rollers with a desired processing step. For centuries the metal industries have also been producing flat products such as metal sheets, plates, strips, bars, etc. through rolling processes. These processes fall in the category of hot or cold *forming* (indicating a net change in the shape of input stock material). Rolling processes

have also been used in cold bonding or welding of metals, and cladding processes (joining of dissimilar metals) [60, 18, 31, 98, 51]. In context to polymers, cold rolling processes have been employed in studying the time-dependent evolution of micro-structural properties after plastic deformation [14], improving the tensile strength and toughness of certain thermoplastics (by unidirectional and biaxial rolling) [13, 12, 55], enhancing the yield strength of cold-forged products [54], and analyzing the tensile properties of rubbers, and (nano)composites [32, 77]. Recently, a new process for manufacturing of pharmaceutical tablets from thin polymeric films has been reported [70, 92, 74, 71, 75, 72], where polymer films are roll-bonded at temperatures well-below their glass transition temperatures. These polymeric films are engineered to exhibit unique mechanical and physical properties, and active plastic deformation triggers requisite molecular mobility to cause macromolecular interdiffusion across polymeric interfaces held in intimate contact, thereby leading to bonding through formation of new entanglements. Such a methodology alleviates the need of adhesives, surface modifications, heat treatments, etc., and is therefore well-suited for pharmaceutical manufacturing. Key requirements for this rolling (bonding) process are: uniform and homogeneous compression of the incoming film-stack at linear feed rates of 5 – 30 mm/min, induction of through-thickness plastic deformation up to 20%, and minimal shearing between the polymeric interfaces during deformation. Details of a rolling machinery to carry out this roll-bonding process are given in [70, 72]. To ensure the product quality and develop a process control for roll-bonding of polymeric films, an accurate and efficient scheme is required for predicting the optimal rolling loads, deformation fields, and resulting stock geometries and properties.

Over the course of the last century there have been extensive theoretical, experimental, and computational efforts to study deformations in rolling processes, and development of models in predicting the forming loads and torques, and distribution of pressures along the arc of contact in the roller bite [81, 82, 30, 97, 46, 61, 45, 63]. Broadly speaking, the methods of analysis for rolling, both analytical and numerical, can be categorized into: (i) slab methods, (ii) slip line analysis, (iii) upper bound analysis, and (iv) computational techniques. Approaches (i)-(iii) make several simplifying approximations on the deformation patterns in the roller bite, and constitutive material behavior, and were largely relied upon when the finite element methods were non-existent. In slab methods the object of deformation is divided into multiple slabs, and for each slab simplifying assumptions are made for the stress distributions. Then, for the resulting system the approximate equilibrium equations are solved with imposition of strain compatibility between the neighboring slabs and boundary tractions, and approximate loads and stress distributions are derived. Often homogeneous compression, constant yield strength, negligible elastic strains, and kinetic friction between the roller and strip are assumed. See [86, 87, 94, 64, 93, 25, 90, 29, 69, 10, 28, 2, 34, 91] for different attempts employing slab methods. Slip line analysis, which also makes assumptions of perfectly-plastic and rate-independent material behavior, yielded only limited success [3, 4, 19, 21] in rolling, and incorporation of realistic frictional or traction

boundary conditions between the stock and the roller remained a challenge. Finally, the upper-bound analysis approaches [9], in which material is again treated as rigid-plastic, and kinematically admissible velocity fields are derived from experimental evidence or experience, have not yielded any greater success. Summarily, the classical techniques are unable to handle geometric and material nonlinearities, rate- and temperature-dependent effects, arbitrary strains in presence of plastic deformation, and complex frictional conditions, and it is to this end modern numerical techniques for solving boundary value problems have emerged as a powerful tool, and have largely superseded these classical approaches. Even though classical techniques cannot capture complexities of an arbitrary rolling process, they are, however, useful sometime in making an order of magnitude estimates for the rolling loads. As we demonstrate in this work, we shall utilize the predictions from rigid-plastic rolling to guide our finite-element analysis.

Finite Element Methods (FEM) have emerged as a powerful computational tool for a variety of purposes. Nowadays most complex, elasto-plastic deformation analyses in solids, where exact analytical solutions are not available, are carried out using FEM. Notable contributions on the development of Total Lagrangian [35], and Updated Lagrangian [56] formulations for the displacement based finite elements, addressing issues related to large deformations and rotations, and material non-linearities, have greatly facilitated the study of metal-forming problems, see [49, 83, 44, 52, 23, 24]. The use of objective stress rate measure has been widely used in nonlinear problems, and plasticity is incorporated through additive decomposition of spatial strain-rate, or multiplicative decomposition of the deformation gradient into the elastic and plastic parts. Locking phenomenon exhibited by the displacement based finite elements due to volume preserving plastic flow constraint in fully plastic regimes has been avoided through special arrangements of the elements [65], or by use of the selective reduced integration method [101]. Other notable approaches of treating material as rigid-plastic, or visco-plastic, and deploying ‘Eulerian’ flow-type formulations, with velocity field as an unknown [17, 99, 20, 100, 58, 40, 37, 68], are not applicable to large strain elasto-plastic analysis of polymer rolling, and are therefore ruled out from further consideration here. A detailed overview of the numerical solutions in context to rolling and forming methods can be found in [41, 84, 22].

While traditional nonlinear elasto-plastic finite element analyses, based on incremental kinematics, employ implicit iterative schemes for solving equilibrium or momentum equations, explicit dynamics-based solution strategies have gained significant popularity in a variety of metal forming applications [79, 39, 53]. Unlike implicit schemes, explicit methods have smaller memory footprint as the storage of tangent stiffness matrix is not required. Explicit integration schemes, however, are only conditionally stable, and the critical time step for stability purposes is approximated as l_e/c , where l_e is the smallest element size and c is the dilatational wave speed, also known as the CFL limit. Explicit dynamics have been quite successful for problems where the inertial effects are negligible, because mass scaling can be adopted to increase the stable time increments, and they also show robust performance in handling contact conditions

(impenetrability and slip/stick), since contact tangent stiffness matrix, as required for implicit methods, is not needed. Another drawback of implicit methods is that the size of the stiffness matrix can change depending upon the contact state, and the stiffness matrix may lose symmetry due to friction. In presence of complex loading and contact conditions, the implicit methods can also face convergence difficulties (even though, when they are successful, they can provide quadratic convergence, and contact conditions can be satisfied exactly using the method of Lagrange multipliers). For explicit methods, predictor-corrector, or penalty based methods are commonly employed to tackle contact conditions.

To best of our knowledge, currently there are no research attempts on efficient and accurate computational modeling of cold rolling of polymers. Thus, in this paper, we resort to the commercial finite element software Abaqus for developing computational procedures to accurately and efficiently model such rolling processes. In general, glassy polymers exhibit a time-dependent viscoplastic mechanical behavior, and therefore quasi-static rolling simulations, adopting a finite deformation time-dependent behavior with sufficiently fine mesh, would require large physical computational times to arrive at a steady-state (long-time) solution. On the other hand, glassy polymers are known to exhibit rate-independent behavior at slow strain-rates and low temperatures [62, 5], and if operating conditions are such that polymer behavior can be modeled without any rate effects, one can make faster computations. For this purpose, using a classical rigid-plastic analysis, we first estimate the upper bound strain rates in the roller-bite, at the specified feed rates, and find that the average strain-rates during rolling are relatively small, so that a rate-independent material model for the polymer films can in fact be adopted. Accordingly, elasto-plastic modeling at large plastic strains with moderate elastic stretches is carried out using formulations based on hypoelasticity, and multiplicative decomposition of deformation gradient into elastic and plastic parts. Consistent with the rate-independent material behavior, Coulombic friction is used between the rollers and polymer films through the kinematic-constraint algorithm. Quasi-static rolling simulations, with the explicit time stepping scheme, and mass-scaling are then used to make predictions for rolling loads.

The rest of the paper is structured as follows: In Section 2, we describe the cold rolling of polymeric films, and utilize a classical rolling model to make preliminary predictions for various deformation fields. Then, a rate-independent polymer deformation model with finite elastic effects, and isotropic hardening is proposed based on hypoelasticity and multiplicative decomposition of deformation gradient in Section 3. Section 4 presents the numerical simulations, and compares the experimentally observed rolling loads with the classical rolling theory, and steady-state finite element rolling simulations. Key features of the deformation mechanics of polymer films in the roller bite are revealed here. Finally, conclusions and directions for future work are summarized in Section 6.

2 Mechanics and Modeling of Cold Roll-Bonding of Solid-State Polymeric Films

2.1 Materials

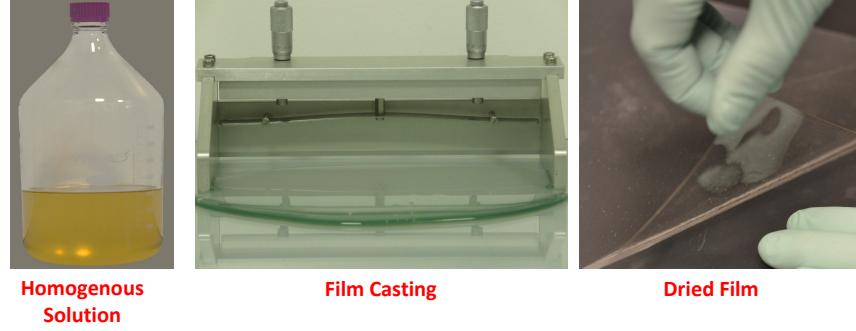


Figure 1: Preparation of polymeric films through solution mixing, film casting, and peeling.

Figure 1 shows synthesis of polymeric films through solvent casting used in this study. Polymer films contained a base polymer METHOCEL E15 and a compatible plasticizer PEG-400. METHOCEL is the trade name for Hydroxypropyl-Methyl-cellulose (HPMC), and PEG-400 is polyethylene glycol with a molecular weight of 400. E15, PEG, ethanol, and water were mixed in a weight ratio of 1.32 : 4.36 : 4.36 : 1, respectively, and a homogeneous solution was obtained through mixing with an electric stirrer for over 24 hours. After completion of the blending process, the solution was carefully stored in glass bottles at rest for 12 hours to get rid of any air bubbles. Solvent casting was carried out using a casting knife applicator from Elcometer on a Heat-resistant Borosilicate Glass. All steps were carried out in a chemical laboratory where ambient conditions of $20^{\circ}\text{C} \pm 2^{\circ}\text{C}$ and R.H. $20\% \pm 5\%$ were noted. After drying, glassy polymeric films of E15 were obtained that contained 42.3% of PEG by weight. The glass transition temperature of the polymeric films was found to be 78°C . Figure 4 shows bonding of multiple layers of films when subjected to plastic deformation in simple compression. See [70, 73] for further details on synthesis, preparation, and characterization of polymeric films, and solid-state bonding through plastic deformation.

A schematic of roll-bonding of multiple polymeric layers is shown in Figure 4, and the actual process is shown in Figure 4. A key requirement in this roll-bonding is to apply sufficient levels of loads to induce through-thickness plastic deformation on the incoming stack of polymer films. The desired levels of plastic strains must be attained over the interval of time τ spent under the compression rollers. The time τ is set by size of the rollers, specified feed rates, and material mechanical response of the films. During active plastic deformation in the roller bite, the polymer molecules interpenetrate across film interfaces and cause bonding. If the stack thickness is *small* compared to the roller radius (R), i.e., $h \ll R$, an element in the roller bite will experience almost homogeneous straining through its thickness, and

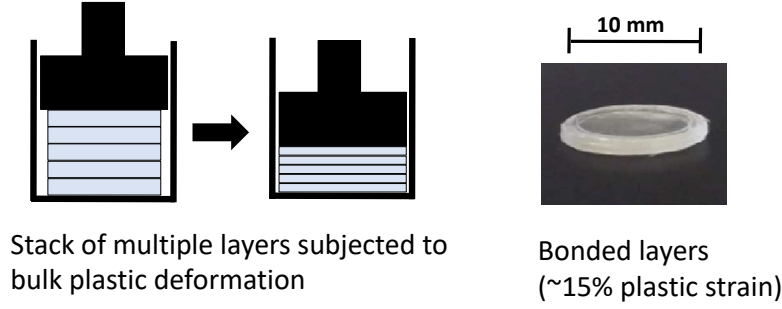


Figure 2: Bonding of polymeric films in compression due to bulk plastic deformation.

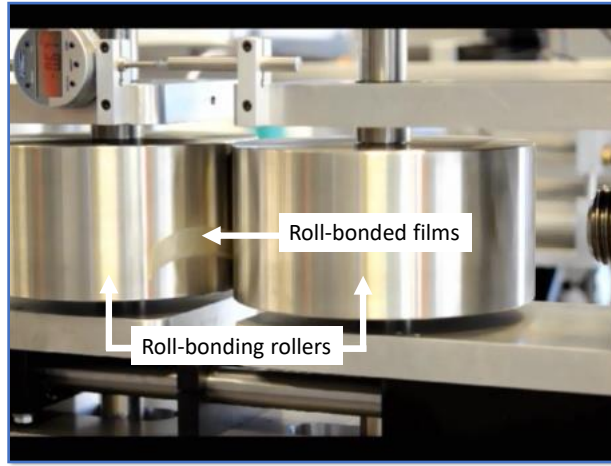


Figure 3: Rolling of polymeric films [70, 72].

negligible shear stresses will develop between the film interfaces. On the other hand, if there is a non-uniform strain across thickness then the interfaces (other than the symmetry plane of the film-stack in thickness direction) will have a tendency to exhibit relative tangential motion, which will hinder molecular interpenetration of polymer chains, and thus diminish bonding. In an extreme limit if the film-stack is quite thick compared to the radius of the rollers, then no through-thickness (plastic) deformation will incur, and only local indentation on polymer films will occur during roller compression. This type of bonding is a multi-scale process in the sense that polymer mobility and interpenetration occurs at a molecular scale, while plastic deformation is triggered at the macroscopic continuum scale. In order to achieve homogeneous and through-thickness plastic deformation, rollers of radius R with $R/h \gg 1$ were selected in the designed machinery [70, 72]. Later through finite element simulations we will verify that under conditions of large roller radii, the through thickness shear stresses are in fact negligible and that the deformation is homogeneous. Next, we resort to a classical analytical model based on rigid-plastic analysis to estimate various fields associated with rolling under prescribed processing conditions, and accordingly make simplifying, yet accurate, assumptions to carry out finite element modeling.

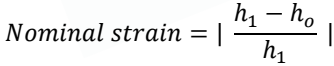


Figure 4: Schematic of a rolling scheme, where multiple layers are fed through rollers and bonded via induced plastic deformation.

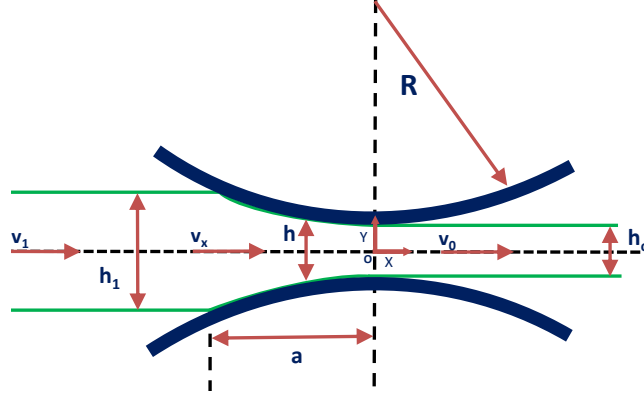


Figure 5: Rigid-perfectly plastic rolling scheme.

2.2 Estimates based on rigid perfectly-plastic material model

A rigid-plastic rolling scheme is shown in Figure 5, see [38] for complete details. In this rolling, the estimates of line loading P_l , and torque M per unit width, into the plane of the figure are given as

$$\frac{P_l}{(\sigma_{y, film}/\sqrt{6})a} = 2 + \frac{a}{h} \left(\frac{1}{2} - \frac{1}{3} \frac{a}{R} \right), \quad (1)$$

and

$$\frac{M}{(\sigma_{y,filim}/\sqrt{6})a^2} = 1 + \frac{a}{4\hbar} \left(1 - \frac{a}{R}\right). \quad (2)$$

In the above equations, $\sigma_{y, film}$ is the yield strength of the material, a is the half contact width, $\bar{h} = \frac{h_1 + h_o}{2}$ is the mean film-stack thickness, and R is the radius of the rollers. From the geometry of deformation, if we assume that there is no slippage or sliding between the rolled-stock and the rollers at the exit, then the exit velocity v_o of the rolled-stock is equal to tangential velocity of the rollers $R\omega$, i.e., $v_o = R\omega$. The

variation of an element height, in the roller bite, as a function of x-coordinate is given as

$$h = h_o + 2R \left(1 - \sqrt{1 - \frac{x^2}{R^2}} \right). \quad (3)$$

The nominal compressive strain in the thickness (or transverse) direction is given as

$$|e_y| = (1 - h/h_1), \quad (4)$$

and accordingly the compressive strain rate is expressed as

$$|\dot{e}_z| = \frac{1}{h_1} \frac{dh}{dt}. \quad (5)$$

From the conservation of mass, during plane strain plastic flow in rolling, we can write

$$v_x h = v_o h_o, \quad (6)$$

where v_x represents the velocity at any section, and thus using the above equations, we can re-write the expression for strain rate as

$$|\dot{e}_z| = \frac{2x h_o v_o}{h_1 h \sqrt{R^2 - x^2}}. \quad (7)$$

In this rolling scheme, if $R/h \gg 1$, the time of compression τ under the rollers can be estimated as

$$\tau = \frac{\sqrt{R(h_i - h_o)}}{v_o}. \quad (8)$$

According to the processing parameters provided in [70, 72], for $\sigma_{y, film} = 6.0$ MPa, $h_1 = 0.6$ mm, $h_o = 0.48$ mm, $2d = (h_1 - h_o) = 0.12$ mm (indicating 20% plastic compression), $R = 100$ mm, and $v_o = 10$ mm/min, we find $\tau = 20.78$ seconds. For these settings the plots of strain rate and strain in the roller-bite are shown in Figures 6 and 7, respectively.

Since we employed a rigid-plastic rolling model in the above calculations, the computed strain rates are overestimates of the actual strain rates that would occur, as the elastic straining is neglected. The strain rates from Figure 6 lie in the range of $10^{-6} - 10^{-5} \text{ s}^{-1}$, and are very small. This is a key observation because solid-state polymers, when deformed at slow to moderate rates, show little rate-sensitivity in their mechanical response, and this simplifies the material modeling task by enabling us to use a rate-independent material model in the finite element simulations. As pointed out in [5], at strain-rates less than 0.01, hardly any rate sensitivity is noted. In fact the rate-dependent models at slow deformation rates reduce to their rate-independent counterparts. If the strain-rate effects are significant, such as in calendaring of elastic-viscous materials [76], then appropriate material behavior models must be considered. At a molecular level, well below the T_g , the resistance to plastic flow in polymers is mostly

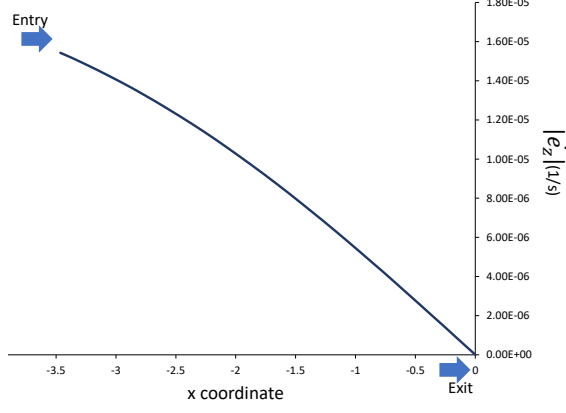


Figure 6: Transverse strain rate plotted as a function of distance from the exit during deformation of film-stack in the rollers. For this case, $h_1 = 0.6$ mm, $h_o = 0.54$ mm (indicating 20% nominal strain in thickness reduction), and $v_o \approx 10.0$ mm/min.

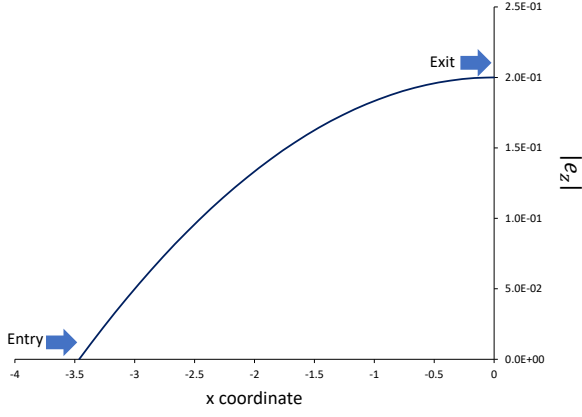


Figure 7: Transverse strain plotted as a function of distance from the exit during deformation of film-stack in the rollers. For this case, $h_1 = 0.6$ mm, $h_o = 0.54$ mm (indicating 20% nominal strain in thickness reduction), and $v_o \approx 10.0$ mm/min.

dominated by the resistance to molecular level re-orientations. The backstress due to entropic chain alignment is dormant well below T_g when only moderately large deformation regimes are considered. Thus, effects due to network elasticity of the polymer matrix can be ignored all together at small to moderately large plastic strains. The plastic flow can be modeled using $J2$ flow criterion and normality flow rule. Pressure sensitivity can also be ignored well below T_g for moderate stress states occurring in rolling. For comprehensive details on the mechanical behavior of polymers see [7]. For popular polymer models see, e.g., [11, 6, 8]. Finally, we also take note of the fact that polymers can exhibit noticeable elastic deformations which cannot be ignored with respect to plastic strains, and our experimental results indeed reveal this behavior.

3 Finite Strain Rate-Independent Elastic-Plastic Material Model for Polymeric Films

Based on the discussions presented in the previous section, we now work towards deriving a rate-independent deformation model to describe the polymer behavior at finite strains. We present two approaches to model this behavior, along with the necessary preliminaries, based on: (a) multiplicative decomposition of deformation gradient into elastic and plastic parts, and (b) hypoelastic formulation that employs an objective measure of stress-rate, and utilizes additive decomposition of spatial strain-rate into elastic and plastic parts.

Kinematics

A homogeneous body B is identified with the region of space that it occupies with respect to a fixed reference configuration. \mathbf{X} denotes an arbitrary material point of B . The motion of B is then described as a smooth one-to-one mapping $\mathbf{x} = \boldsymbol{\chi}(\mathbf{X}, t)$, and the deformation gradient is defined as

$$\mathbf{F} = \nabla \boldsymbol{\chi} = \frac{\partial \boldsymbol{\chi}}{\partial \mathbf{X}}. \quad (9)$$

The velocity gradient \mathbf{L} , i.e., gradient of the spatial velocity with respect to spatial coordinates, is related to the deformation gradient \mathbf{F} through the identity

$$\mathbf{L} = \text{grad } \dot{\boldsymbol{\chi}} = \dot{\mathbf{F}} \mathbf{F}^{-1} \quad (10)$$

The velocity gradient \mathbf{L} can be decomposed into the symmetric part \mathbf{D} and anti-symmetric part \mathbf{W} as

$$\mathbf{D} = \frac{1}{2} [\mathbf{L} + \mathbf{L}^T], \quad (11)$$

and

$$\mathbf{W} = \frac{1}{2} [\mathbf{L} - \mathbf{L}^T]. \quad (12)$$

\mathbf{D} is the stretching rate tensor and \mathbf{W} is the continuum spin. Within the framework of large deformations, the multiplicative decomposition [43] of the deformation gradient \mathbf{F} can be written as

$$\mathbf{F} = \mathbf{F}^e \mathbf{F}^p, \quad (13)$$

where \mathbf{F}^e represents the local elastic deformation of material in an infinitesimal neighborhood of \mathbf{X} due to stretch and rotation. \mathbf{F}^p is the plastic distortion and represents the local deformation of material \mathbf{X} in an infinitesimal neighborhood due to the irreversible or plastic deformation. By substituting \mathbf{F} from Equation 13 into Equation 10, we can obtain the following expression for \mathbf{L} as

$$\mathbf{L} = \dot{\mathbf{F}}^e \mathbf{F}^{e-1} + \mathbf{F}^e \dot{\mathbf{F}}^p \mathbf{F}^{p-1} \mathbf{F}^{e-1}. \quad (14)$$

We define the elastic and plastic velocity gradients, \mathbf{L}^e and \mathbf{L}^p , as follows

$$\mathbf{L}^e = \dot{\mathbf{F}}^e \mathbf{F}^{e-1}, \quad (15)$$

and

$$\mathbf{L}^p = \dot{\mathbf{F}}^p \mathbf{F}^{p-1}. \quad (16)$$

Using Equations 15 and 16, we can rewrite Equation 14 as

$$\mathbf{L} = \mathbf{L}^e + \mathbf{F}^e \mathbf{L}^p \mathbf{F}^{e-1}. \quad (17)$$

Now the elastic stretching \mathbf{D}^e and the elastic spin \mathbf{W}^e are defined as

$$\mathbf{D}^e = \frac{1}{2}[\mathbf{L}^e + \mathbf{L}^{e\top}], \quad (18)$$

and

$$\mathbf{W}^e = \frac{1}{2}[\mathbf{L}^e - \mathbf{L}^{e\top}]. \quad (19)$$

Similarly, the plastic stretching \mathbf{D}^p and the plastic spin \mathbf{W}^p are defined as

$$\mathbf{D}^p = \frac{1}{2}[\mathbf{L}^p + \mathbf{L}^{p\top}], \quad (20)$$

and

$$\mathbf{W}^p = \frac{1}{2}[\mathbf{L}^p - \mathbf{L}^{p\top}]. \quad (21)$$

We shall utilize two commonly employed kinematical assumptions concerning the plastic flow. First, the plastic flow is incompressible, i.e., plastic flow does not induce volume changes. This condition is achieved by assuming that \mathbf{L}^p and hence \mathbf{D}^p are deviatoric, i.e., $\text{tr}(\mathbf{L}^p) = \text{tr}(\mathbf{D}^p) = 0$. This condition can be expressed as

$$J^p = \det \mathbf{F}^p = 1 \quad \text{and} \quad \text{tr} \mathbf{L}^p = 0. \quad (22)$$

We can also decompose $J = \det \mathbf{F}$ into elastic and plastic components as $J = \det \mathbf{F}^e \det \mathbf{F}^p$. Using $J^e = \det \mathbf{F}^e$ and $J^p = \det \mathbf{F}^p = 1$, we have $J = J^e J^p = J^e$. Secondly, if we idealize the material to be isotropic, then plastic flow can be assumed to be irrotational [33], i.e.,

$$\mathbf{W}^p = \mathbf{0}. \quad (23)$$

Accordingly, \mathbf{L}^p is symmetric and

$$\mathbf{D}^p = \mathbf{L}^p. \quad (24)$$

From Equation 16, we can write

$$\mathbf{D}^p = \mathbf{L}^p = \dot{\mathbf{F}}^p \mathbf{F}^{p-1}. \quad (25)$$

Rearranging the terms in Equation 25, we obtain

$$\dot{\mathbf{F}}^p = \mathbf{D}^p \mathbf{F}^p. \quad (26)$$

The deformation gradient \mathbf{F} admits a right and left polar decomposition given as

$$\mathbf{F} = \mathbf{R}\mathbf{U} = \mathbf{V}\mathbf{R}. \quad (27)$$

The polar decomposition for the elastic and plastic part of deformation gradient can also be carried out as

$$\mathbf{F}^e = \mathbf{R}^e \mathbf{U}^e = \mathbf{V}^e \mathbf{R}^e, \quad (28)$$

and

$$\mathbf{F}^p = \mathbf{R}^p \mathbf{U}^p = \mathbf{V}^p \mathbf{R}^p. \quad (29)$$

In what follows, we assume that the plastic part of the deformation gradient, i.e., \mathbf{F}^p (and therefore \mathbf{L}^p) is invariant under frame transformation. This is a common approach [6, 33], and simply implies that the fictitious intermediate configuration, which is obtained by elastic destressing, of a material point neighborhood, is invariant. \mathbf{F}^p is a point wise map of each material point neighborhood from the reference configuration to the intermediate configuration (due to plastic distortion alone), and its invariance under the change of the observer can be assumed without the loss of generality; granted that the remaining kinematics of deformation is then described consistently under this assumption.

3.1 Rate-Independent Deformation Model Based on Multiplicative Decomposition of Deformation Gradient

Multiplicative decomposition of deformation gradient into elastic and plastic parts was first introduced in [42] and [43], and has gained wide popularity in modeling constitutive responses of variety of materials. In this section we summarize a deformation model based on the multiplicative decomposition, list the constitutive equations, and also provide the time integration algorithm.

Consider B to be the reference body. P be an arbitrary part of the reference body which is represented by P_t at any time t . \mathbf{n} is the outward unit normal on the boundary of P_t . Let the traction field be represented by \mathbf{t} (with the associated unit vector \mathbf{n}) and the body force by \mathbf{b}_0 . Accordingly, the body

force including the effect of inertia can be written as

$$\mathbf{b} = \mathbf{b}_0 - \rho \ddot{\boldsymbol{\chi}}. \quad (30)$$

Both \mathbf{t} and \mathbf{b} expend power over the velocity $\dot{\boldsymbol{\chi}}$, and the rate of external work can be written as

$$\mathcal{W}(P_t) = \int_{\partial P_t} \mathbf{t}(\mathbf{n}) \cdot \dot{\boldsymbol{\chi}} da + \int_{P_t} \mathbf{b} \cdot \dot{\boldsymbol{\chi}} dv. \quad (31)$$

Now we assume that the internal power inside the body is expended against two internal kinematical processes during deformation, elastic and plastic, and corresponding “micro-stresses” arising due to these processes are:

- An elastic stress \mathbf{S}^e (defined in the current configuration) that is power-conjugate to \mathbf{L}^e . Thus, the power expended per unit volume of the current configuration is $\mathbf{S}^e : \mathbf{L}^e$.
- A plastic stress \mathbf{T}^p (defined in the intermediate configuration) which is power-conjugate to \mathbf{L}^p . Thus, the power expended per unit volume in the intermediate configuration is $\mathbf{T}^p : \mathbf{L}^p$. Since \mathbf{L}^p is deviatoric, we assume that \mathbf{T}^p is also deviatoric.

We note that the fictitious intermediate configuration and the reference configuration have same volume (due to plastic incompressibility). Thus, the total internal power expended in the body can be expressed as a volume integral over the current configuration as

$$\mathcal{J}(P_t) = \int_{P_t} (\mathbf{S}^e : \mathbf{L}^e + J^{-1} \mathbf{T}^p : \mathbf{L}^p) dv. \quad (32)$$

3.1.1 Principal of virtual power

Let us consider that at any given fixed time, the deformation fields $\boldsymbol{\chi}$ and \mathbf{F}^e (hence \mathbf{F} and \mathbf{F}^p) are given. Now the virtual velocities corresponding to the fields \mathbf{v} , \mathbf{L}^e and \mathbf{L}^p be represented as the set $\mathcal{V} = (\tilde{\mathbf{v}}, \tilde{\mathbf{L}}^e, \tilde{\mathbf{L}}^p)$. According to Equation 17, the kinematically admissible virtual quantities must satisfy the following constraint

$$\text{grad} \tilde{\mathbf{v}} = \tilde{\mathbf{L}}^e + \mathbf{F}^e \tilde{\mathbf{L}}^p \mathbf{F}^{e-1}. \quad (33)$$

Then, according to Equations 31 and 32 we can write the external virtual power as

$$\mathcal{W}(P_t, \mathcal{V}) = \int_{\partial P_t} \mathbf{t}(\mathbf{n}) \cdot \tilde{\mathbf{v}} da + \int_{P_t} \mathbf{b} \cdot \tilde{\mathbf{v}} dv, \quad (34)$$

and the internal virtual work as

$$\mathcal{J}(P_t, \mathcal{V}) = \int_{P_t} (\mathbf{S}^e : \tilde{\mathbf{L}}^e + J^{-1} \mathbf{T}^p : \tilde{\mathbf{L}}^p) dv. \quad (35)$$

According to the principle of virtual work, given any part P , $\mathcal{W}(P_t, \mathcal{V}) = \mathcal{J}(P_t, \mathcal{V})$ for all generalized and kinematically admissible virtual velocities \mathcal{V} , i.e.,

$$\int_{\partial P_t} \mathbf{t}(\mathbf{n}) \cdot \tilde{\mathbf{v}} da + \int_{P_t} \mathbf{b} \cdot \tilde{\mathbf{v}} dv = \int_{P_t} (\mathbf{S}^e : \tilde{\mathbf{L}}^e + J^{-1} \mathbf{T}^p : \tilde{\mathbf{L}}^p) dv. \quad (36)$$

In other words, the assumption (or choice) of work conjugate stress measures \mathbf{S}^e and \mathbf{T}^p is justified, if and only if, they satisfy Equation 36 for all kinematically admissible virtual velocities constrained by the Equation 33.

3.1.2 Consequences of frame indifference

Based on the physical grounds, we require that the internal (virtual) work $\mathcal{J}(P_t, \mathcal{V})$ (Equation 35), which is a scalar quantity, must be invariant under a change of reference frame. Given a change in frame, if P_t^* and $\mathcal{J}^*(P_t^*, \mathcal{V}^*)$ represent the region and the internal work in the new frame, then the invariance of the internal work requires

$$\mathcal{J}(P_t, \mathcal{V}) = \mathcal{J}^*(P_t^*, \mathcal{V}^*), \quad (37)$$

where \mathcal{V}^* is the kinematically admissible virtual velocity in the new frame. Also transformation of the virtual fields upon the change of reference follows identically their nonvirtual counterparts. Further from standard transformation laws under change of reference frame, we can write

$$\tilde{\mathbf{L}}^{e*} = \mathbf{Q} \tilde{\mathbf{L}}^e \mathbf{Q}^\top + \mathbf{\Omega}, \quad (38)$$

where $\tilde{\mathbf{L}}^{e*}$ is the elastic distortion rate in the new frame, \mathbf{Q} is the frame-rotation, and $\mathbf{\Omega} = \dot{\mathbf{Q}} \mathbf{Q}^\top$ is the frame-spin. Since, we have taken \mathbf{F}^p to be frame invariant under change of frame, thus, according to Equation 16 \mathbf{L}^p is frame invariant, and so is $\tilde{\mathbf{L}}^p$. If we consider a virtual field with $\tilde{\mathbf{L}}^p = \mathbf{0}$, then the invariance of internal virtual work Equations 35 and 37 reduces to

$$\int_{P_t} (\mathbf{S}^e : \tilde{\mathbf{L}}^e) dv = \int_{P_t^*} (\mathbf{S}^{e*} : \tilde{\mathbf{L}}^{e*}), dv^*, \quad (39)$$

i.e., internal virtual work due to \mathbf{S}^e must be invariant. In Equation 39, $dv = dv^*$ (since differential volume is unaffected upon change of reference), the integral on the right hand side can be transformed over P_t , and since P_t is arbitrary the following should be satisfied pointwise

$$\mathbf{S}^e : \tilde{\mathbf{L}}^e = \mathbf{S}^{e*} : \tilde{\mathbf{L}}^{e*}. \quad (40)$$

Substituting $\tilde{\mathbf{L}}^{e*}$ from Equation 38 into the right hand side of Equation 40, we obtain

$$\mathbf{S}^e : \tilde{\mathbf{L}}^e = \mathbf{S}^{e*} : \mathbf{Q} \tilde{\mathbf{L}}^e \mathbf{Q}^\top + \mathbf{S}^{e*} : \boldsymbol{\Omega}. \quad (41)$$

If we choose a frame whose spin $\boldsymbol{\Omega}$ is zero then above equation reduces to

$$\mathbf{S}^e : \tilde{\mathbf{L}}^e = \mathbf{S}^{e*} : \mathbf{Q} \tilde{\mathbf{L}}^e \mathbf{Q}^\top, \quad (42)$$

or

$$\mathbf{S}^e : \tilde{\mathbf{L}}^e = \mathbf{Q}^\top \mathbf{S}^{e*} \mathbf{Q} : \tilde{\mathbf{L}}^e. \quad (43)$$

Since Equation 43 must hold true for all kinematically admissible $\tilde{\mathbf{L}}^e$, we conclude that

$$\mathbf{S}^{e*} = \mathbf{Q} \mathbf{S}^e \mathbf{Q}^\top. \quad (44)$$

Further, if we choose a rotating frame with $\mathbf{Q} = \mathbf{I}$, i.e., a frame that instantaneously coincides with the reference frame but with a non-zero spin then $\mathbf{S}^{e*} = \mathbf{S}^e$ at that instant, and Equation 42 reduces to

$$\mathbf{S}^e : \boldsymbol{\Omega} = 0. \quad (45)$$

Since $\boldsymbol{\Omega}$ is arbitrary and skew, therefore Equation 45 is satisfied for all $\boldsymbol{\Omega}$, if and only if, $\mathbf{S}^e = \mathbf{S}^{eT}$. So far we utilized the fact that internal virtual work due to elastic stretching must be invariant by choosing $\tilde{\mathbf{L}}^p = 0$, which is justified in an elastic-plastic constitutive model if one imagines deformation processes in the elastic regime only. The invariance of elastic part of the internal virtual work implies that plastic part of the internal virtual work must also be invariant, and since $\tilde{\mathbf{L}}^p$ is invariant so should $\tilde{\mathbf{T}}^p$ be.

3.1.3 Macroscopic force balance

We again consider a macroscopic virtual velocity \mathcal{V} for which $\tilde{\mathbf{v}}$ is arbitrary and $\tilde{\mathbf{L}}^e = \text{grad} \tilde{\mathbf{v}}$, with $\tilde{\mathbf{L}}^p = 0$. By substituting $\tilde{\mathbf{L}}^p = 0$ in Equation 35 and equating equations 34 and 35, we obtain

$$\int_{\partial P_t} \mathbf{t}(\mathbf{n}) \cdot \tilde{\mathbf{v}} da + \int_{P_t} \mathbf{b} \cdot \tilde{\mathbf{v}} dv = \int_{P_t} (\mathbf{S}^e : \tilde{\mathbf{L}}^e) dv. \quad (46)$$

By using divergence theorem, we can rewrite the right hand term of the equation 46 as

$$\int_{P_t} (\mathbf{S}^e : \tilde{\mathbf{L}}^e) dv = - \int_{P_t} \text{div} \mathbf{S}^e \cdot \tilde{\mathbf{v}} dv + \int_{\partial P_t} (\mathbf{S}^e \mathbf{n}) \cdot \tilde{\mathbf{v}} da. \quad (47)$$

Therefore, Equation 46 becomes

$$\int_{\partial P_t} \mathbf{t}(\mathbf{n}) \cdot \tilde{\mathbf{v}} da + \int_{P_t} \mathbf{b} \cdot \tilde{\mathbf{v}} dv = - \int_{P_t} \text{div} \mathbf{S}^e \cdot \tilde{\mathbf{v}} dv + \int_{\partial P_t} (\mathbf{S}^e \mathbf{n}) \cdot \tilde{\mathbf{v}} da, \quad (48)$$

upon re-writing

$$\int_{\partial P_t} (\mathbf{t}(\mathbf{n}) - \mathbf{S}^e \mathbf{n}) \cdot \tilde{\mathbf{v}} da + \int_{P_t} (\operatorname{div} \mathbf{S}^e + \mathbf{b}) \cdot \tilde{\mathbf{v}} dv = 0. \quad (49)$$

Since, Equation 49 must hold for all P and all $\tilde{\mathbf{v}}$, the traction condition yields to

$$\mathbf{t}(\mathbf{n}) = \mathbf{S}^e \mathbf{n}, \quad (50)$$

and the local force balance

$$\operatorname{div} \mathbf{S}^e + \mathbf{b} = \mathbf{0}. \quad (51)$$

This traction condition and the force balance and the symmetry, and frame-indifference of \mathbf{S}^e are classical conditions satisfied by the Cauchy stress \mathbf{T} , an observation that allow us to write

$$\mathbf{T} \stackrel{def}{=} \mathbf{S}^e, \quad (52)$$

and to view

$$\mathbf{T} = \mathbf{T}^\top \quad (53)$$

as the macroscopic stress and as the local macroscopic force balance. Granted that we are working in an inertial frame, so that Equation 51 reduces to the local balance law for linear momentum

$$\operatorname{div} \mathbf{T} + \mathbf{b}_0 = \rho \dot{\mathbf{v}}, \quad (54)$$

where \mathbf{b}_0 is the non-inertial body force.

3.1.4 Microscopic force balance

Now we assume virtual fields \mathcal{V} such that $\tilde{\mathbf{v}} = 0$. Then according to Equation 33 we have

$$\tilde{\mathbf{L}}^e = -\mathbf{F}^e \tilde{\mathbf{L}}^p \mathbf{F}^{e-1}. \quad (55)$$

Similarly, Equation 36 reduces to

$$\int_{P_t} (\mathbf{T} : \tilde{\mathbf{L}}^e + J^{-1} \mathbf{T}^p : \tilde{\mathbf{L}}^p) dv = 0, \quad (56)$$

for all P_t . This implies that quantity inside the integral is identically zero, i.e.,

$$J^{-1} \mathbf{T}^p : \tilde{\mathbf{L}}^p = -\mathbf{T} : \tilde{\mathbf{L}}^e. \quad (57)$$

Now substituting $\tilde{\mathbf{L}}^e$ from Equation 55 into Equation 57 we obtain

$$J^{-1} \mathbf{T}^p : \tilde{\mathbf{L}}^p = \mathbf{T} : (\mathbf{F}^e \tilde{\mathbf{L}}^p \mathbf{F}^{e-1}). \quad (58)$$

By performing some algebraic manipulation and utilizing the fact that $\tilde{\mathbf{L}}^p$ is deviatoric and \mathbf{T} is symmetric, we find that

$$J^{-1} \mathbf{T}^p : \tilde{\mathbf{L}}^p = (\mathbf{F}^{e\top} \mathbf{T}_0 \mathbf{F}^{e-\top}) : \tilde{\mathbf{L}}^p. \quad (59)$$

Since $\tilde{\mathbf{L}}^p$ is arbitrary, the microscopic force balance leads to

$$J \mathbf{F}^{e\top} \mathbf{T}_0 \mathbf{F}^{e-\top} = \mathbf{T}^p. \quad (60)$$

Next, we define the Mandel stress as

$$\mathbf{M}^e \stackrel{def}{=} J \mathbf{F}^{e\top} \mathbf{T} \mathbf{F}^{e-\top} \quad (61)$$

We note that

$$\mathbf{T}^p = \mathbf{M}_0^e. \quad (62)$$

3.1.5 Rate-independent elastic-plastic constitutive response

We denote the free energy per unit volume of the intermediate configuration as φ , and make a constitutive hypothesis that it only depends on the elastic part of the deformation \mathbf{F}^e . Further, if we invoke the requirement of the frame invariance of free energy (which it must satisfy due to being a scalar quantity), then we can deduce

$$\varphi = \hat{\varphi}(\mathbf{C}^e). \quad (63)$$

Following the standard and well accepted principle of free-energy imbalance in solids [16], during the deformation, where $\mathcal{W}(P_t) = \mathcal{J}(P_t)$, we require that

$$\int_{P_t} \dot{\varphi} J^{-1} dv - \int_{P_t} (\mathbf{T} : \mathbf{L}^e + J^{-1} \mathbf{T}^p : \mathbf{L}^p) dv \leq 0. \quad (64)$$

Since P_t is arbitrary the above equation implies

$$\dot{\varphi} - J \mathbf{T} : \mathbf{L}^e - \mathbf{T}^p : \mathbf{L}^p = -\delta \leq 0, \quad (65)$$

where δ is the dissipation magnitude. We note that \mathbf{T} is symmetric, thus

$$\mathbf{T} : \mathbf{L}^e = \mathbf{T} : \mathbf{D}^e. \quad (66)$$

By defining

$$\mathbf{T}^e \stackrel{def}{=} J \mathbf{F}^{e-1} \mathbf{T} \mathbf{F}^{e-\top}, \quad (67)$$

we can show that

$$J \mathbf{T} : \mathbf{D}^e = \frac{1}{2} \mathbf{T}^e : \dot{\mathbf{C}}^e. \quad (68)$$

Also, using the definition of \mathbf{M}^e from Equation 61 and that of \mathbf{T}^e from Equation 67 we obtain

$$\mathbf{M}^e = \mathbf{C}^e \mathbf{T}^e. \quad (69)$$

Using Equation 63 we can write

$$\dot{\varphi} = \frac{\partial \hat{\varphi}(\mathbf{C}^e)}{\partial \mathbf{C}^e} : \dot{\mathbf{C}}^e \quad (70)$$

and, now using Equations 66, 68 and 70 in Equation 65, the free-energy imbalance can be written as

$$\left[\frac{1}{2} \mathbf{T}^e - \frac{\partial \hat{\varphi}(\mathbf{C}^e)}{\partial \mathbf{C}^e} \right] : \dot{\mathbf{C}}^e + \mathbf{T}^p : \mathbf{L}^p \geq 0. \quad (71)$$

If we consider kinematical processes in which $\mathbf{L}^p = \mathbf{0}$ and

$$\dot{\mathbf{C}}^e = -\kappa \left[\frac{1}{2} \mathbf{T}^e - \frac{\partial \hat{\varphi}(\mathbf{C}^e)}{\partial \mathbf{C}^e} \right], \quad (72)$$

where κ is some positive constant then Equation 71 reduces to

$$-\kappa \left[\frac{1}{2} \mathbf{T}^e - \frac{\partial \hat{\varphi}(\mathbf{C}^e)}{\partial \mathbf{C}^e} \right] : \left[\frac{1}{2} \mathbf{T}^e - \frac{\partial \hat{\varphi}(\mathbf{C}^e)}{\partial \mathbf{C}^e} \right] \geq 0. \quad (73)$$

The only possible way to satisfy equation 73, for arbitrary pair of nonzero \mathbf{T}^e and $\frac{\partial \hat{\varphi}(\mathbf{C}^e)}{\partial \mathbf{C}^e}$, is to have

$$\mathbf{T}^e = 2 \frac{\partial \hat{\varphi}(\mathbf{C}^e)}{\partial \mathbf{C}^e}. \quad (74)$$

An immediate consequence of Equation 74 in conjunction with Equation 71 is that

$$\mathbf{T}^p : \mathbf{L}^p \geq 0. \quad (75)$$

Equation 75 is satisfied for all possible combinations of \mathbf{T}^p and \mathbf{L}^p , if and only if, the deviatoric plastic velocity gradient is colinear with \mathbf{T}^p . To proceed further, we need to specify the form of free energy function. If we assume that the material remains isotropic during deformation, then the dependence of the free energy φ reduces to only the invariants of \mathbf{C}^e , i.e.

$$\varphi = \tilde{\varphi}(\mathcal{I}_{\mathbf{C}^e}), \quad (76)$$

where $\mathcal{I}_{\mathbf{C}^e} = (I_1(\mathbf{C}^e), I_2(\mathbf{C}^e), I_3(\mathbf{C}^e))$ is set of invariants of \mathbf{C}^e . The spectral decomposition of \mathbf{C}^e can

be written as

$$\mathbf{C}^e = \sum_{i=1}^3 \omega_i^e \mathbf{r}_i^e \otimes \mathbf{r}_i^e, \quad \text{with} \quad \omega_i^e = \lambda_i^{e2}, \quad (77)$$

where $(\mathbf{r}_1^e, \mathbf{r}_2^e, \mathbf{r}_3^e)$ are the orthonormal eigenvectors of \mathbf{C}^e and \mathbf{U}^e , and $(\lambda_1^e, \lambda_2^e, \lambda_3^e)$ are the positive eigenvalues of \mathbf{U}^e . The free energy function 76 can then be written as a function of λ_1^e , λ_2^e and λ_3^e , i.e.,

$$\varphi = \hat{\psi}(\lambda_1^e, \lambda_2^e, \lambda_3^e). \quad (78)$$

Using Equation 74 and chain rule of differential we can write

$$\mathbf{T}^e = 2 \frac{\partial \hat{\psi}(\lambda_1^e, \lambda_2^e, \lambda_3^e)}{\partial \mathbf{C}^e} = 2 \sum_{i=1}^3 \frac{\partial \hat{\psi}(\lambda_1^e, \lambda_2^e, \lambda_3^e)}{\partial \lambda_i^e} \frac{\partial \lambda_i^e}{\partial \mathbf{C}^e} = \sum_{i=1}^3 \frac{1}{\lambda_i^e} \frac{\partial \hat{\psi}(\lambda_1^e, \lambda_2^e, \lambda_3^e)}{\partial \lambda_i^e} \frac{\partial \omega_i}{\partial \mathbf{C}^e}. \quad (79)$$

Using Equation 77 into Equation 79, it can be proved that

$$\frac{\partial \omega_i^e}{\partial \mathbf{C}^e} = \mathbf{r}_i^e \otimes \mathbf{r}_i^e, \quad (80)$$

and now using Equations 80 and 79 we obtain

$$\mathbf{T}^e = \sum_{i=1}^3 \frac{1}{\lambda_i^e} \frac{\partial \hat{\psi}(\lambda_1^e, \lambda_2^e, \lambda_3^e)}{\partial \lambda_i^e} \mathbf{r}_i^e \otimes \mathbf{r}_i^e. \quad (81)$$

Using Equation 67, we can now find the Cauchy stress \mathbf{T} as

$$\mathbf{T} = J^{-1} \mathbf{F}^e \mathbf{T}^e \mathbf{F}^{e\top} = J^{-1} \mathbf{R}^e \mathbf{U}^e \mathbf{T}^e \mathbf{U}^e \mathbf{R}^{e\top} = J^{-1} \mathbf{R}^e \left(\sum_{i=1}^3 \lambda_i^e \frac{\partial \hat{\psi}(\lambda_1^e, \lambda_2^e, \lambda_3^e)}{\partial \lambda_i^e} \mathbf{r}_i^e \otimes \mathbf{r}_i^e \right) \mathbf{R}^{e\top}. \quad (82)$$

Similarly, using Equation 69 we can obtain an expression for \mathbf{M}^e as

$$\mathbf{M}^e = \sum_{i=1}^3 \lambda_i^e \frac{\partial \hat{\psi}(\lambda_1^e, \lambda_2^e, \lambda_3^e)}{\partial \lambda_i^e} \mathbf{r}_i^e \otimes \mathbf{r}_i^e. \quad (83)$$

Next, we define a measure of elastic strain \mathbf{E}^e as

$$\mathbf{E}^e \stackrel{def}{=} \ln \mathbf{U}^e = \sum_{i=1}^3 E_i^e \mathbf{r}_i^e \otimes \mathbf{r}_i^e \quad (84)$$

where,

$$E_i^e \stackrel{def}{=} \ln \lambda_i^e. \quad (85)$$

The free energy function can now be re-written in terms of E_1^e , E_2^e and E_3^e as

$$\varphi = \hat{\psi}(\lambda_1^e, \lambda_2^e, \lambda_3^e) = \psi(E_1^e, E_2^e, E_3^e). \quad (86)$$

$$\mathbf{M}^e = \sum_{i=1}^3 \frac{\partial \psi(E_1^e, E_2^e, E_3^e)}{\partial E_i^e} \mathbf{r}_i^e \otimes \mathbf{r}_i^e. \quad (87)$$

A popular choice for free energy form that is valid for moderately large elastic deformation is as follows

$$\psi(\mathbf{E}^e) = G|\mathbf{E}_0^e|^2 + \frac{1}{2}K(\text{tr}\mathbf{E}^e)^2, \quad (88)$$

where G is the shear modulus and K is the bulk modulus. If Young's modulus E and Poisson's ratio ν are known, then bulk and shear modulus are obtained from following relations

$$G = \frac{E}{2(1 + \nu)}, \quad (89)$$

$$K = \frac{2G\nu}{1 - 2\nu}. \quad (90)$$

The free energy is an isotropic function of \mathbf{E}^e (satisfying frame invariance and material isotropy). From Equations 88 and 87, we obtain an expression for Mandel stress in terms of \mathbf{E}^e as

$$\mathbf{M}^e = 2G\mathbf{E}_0^e + K(\text{tr}\mathbf{E}^e)\mathbf{I}. \quad (91)$$

Using the relation in Equation 67, now we can obtain the Cauchy stress in the current configuration as

$$\mathbf{T} = J^{-1} \mathbf{R}^e \mathbf{M}^e \mathbf{R}^{e\top}. \quad (92)$$

We note that the free energy, Equation 88, based on Hencky strain measure does not satisfy the property of polyconvexity, a sufficient condition for existence of minimizers for problems of nonlinear elasticity, see [57, 66, 88]; however, for small to moderately large strains in problems of nonlinear elasticity, and large strain plasticity of glassy polymers, its use has proven to be extremely effective.

3.1.6 Plastic flow: yield and consistency condition

Recall that earlier in Section 3.1, we defined \mathbf{T}^p as the work conjugate to plastic flow which is characterized by \mathbf{L}^p (or \mathbf{D}^p). Now we require a condition to determine the onset of yielding or active plastic flow. To this end, the yield surface is represented with a spherical surface of radius $Y(e^p) > 0$ in the space of symmetric and deviatoric tensors. Here e^p indicates the accumulated plastic strain, and radius of the yield surface depends on it. The elastic range then identified as the closed ball with the radius $Y(e^p)$. Plastic flow can only happen when \mathbf{T}^p lies on the yield surface. From Equation 62 we have $|\mathbf{M}_0^e| = |\mathbf{T}^p|^{-1}$, and thus condition for yielding can be written as

$$|\mathbf{M}_0^e| = Y(e^p) \quad \text{for} \quad \mathbf{D}^p \neq 0, \quad (93)$$

¹In our notation, the $|\mathbf{A}|$ of a tensor \mathbf{A} is equal to $\sqrt{\frac{3}{2}\mathbf{A}:\mathbf{A}}$

and the condition

$$\mathbf{D}^p = 0 \quad \text{for} \quad |\mathbf{M}_0^e| < Y(e^p). \quad (94)$$

We introduce a scalar yield function

$$f = |\mathbf{M}_0^e| - Y(e^p), \quad (95)$$

and f follows the following constraint

$$-Y(e^p) \leq f \leq 0. \quad (96)$$

The yield condition in Equation 93 is then equivalent to the requirement that

$$f = 0 \quad \text{for} \quad \mathbf{D}^p \neq 0, \quad (97)$$

and Equation 94 takes the form

$$\mathbf{D}^p = 0 \quad \text{for} \quad f < 0. \quad (98)$$

The yield function f obeys the following additional restriction:

$$\text{if } f = 0 \quad \text{then} \quad \dot{f} \leq 0. \quad (99)$$

This leads to the no-flow condition

$$\mathbf{D}^p = 0 \quad \text{if } f < 0 \quad \text{or if } f = 0 \quad \text{and} \quad \dot{f} < 0, \quad (100)$$

and the consistency condition

$$\text{if } \mathbf{D}^p \neq 0, \quad \text{then} \quad f = 0 \quad \text{and} \quad \dot{f} = 0. \quad (101)$$

Next, let

$$Y'(e^p) = \frac{dY(e^p)}{de^p}, \quad (102)$$

so that by Equation 97

$$\overline{\dot{Y}(e^p)} = Y'(e^p)|\mathbf{D}^p|; \quad (103)$$

then, letting

$$H(e^p) \stackrel{def}{=} Y'(e^p), \quad (104)$$

we arrive at

$$\overline{\dot{Y}(e^p)} = H(e^p)|\mathbf{D}^p|. \quad (105)$$

Thus, if we assume that $\mathbf{D}^p \neq 0$, then by Equation 93, $|\mathbf{M}_0^e| - Y(e^p) = 0$, hence Equation 105 yields

$$\overline{\dot{|\mathbf{M}_0^e|}} = H(e^p)|\mathbf{D}^p|. \quad (106)$$

First of all, a consequence of flow rule is that

$$\mathbf{N}^p = \frac{\mathbf{M}_0^e}{|\mathbf{M}_0^e|}, \quad (107)$$

i.e., the deviatoric Mandel tensor points in the direction of plastic flow. During plastic flow we have

$$\dot{f} = \overline{\dot{\mathbf{M}}_0^e} - \overline{Y(e^p)}, \quad (108)$$

$$\dot{f} = \frac{\mathbf{M}_0^e}{|\mathbf{M}_0^e|} : \dot{\mathbf{M}}_0^e - H(e^p) |\mathbf{D}^p|, \quad (109)$$

$$\dot{f} = \mathbf{N}^p : \dot{\mathbf{M}}_0^e - H(e^p) |\mathbf{D}^p|. \quad (110)$$

Our next step is to compute the term $\mathbf{N}^p : \dot{\mathbf{M}}_0^e$. Clearly,

$$\mathbf{N}^p : \dot{\mathbf{M}}_0^e = \mathbf{N}^p : \dot{\mathbf{M}}^e, \quad (111)$$

because \mathbf{N}^p is deviatoric.

3.1.7 Time Integration for Rate-Independent Multiplicative Plasticity

Now we describe the time integration for the rate-independent and isotropic hardening deformation model with the multiplicative decomposition of the deformation gradient. The structure adopted here is that of a deformation driven problem, i.e., at each integration point of the finite element an updated deformation gradient is provided, and we are required to compute all the desired quantities. Most quantities are updated explicitly, however, the yield condition (and associated consistency parameter) are solved iteratively.

Initialization: At time step $n = 0$,

Compute the volume ratio J_{n+1} using

$$J_{n+1} = \det(\mathbf{F}_{n+1}). \quad (112)$$

Initialize $\mathbf{N}^p = 0$, $\Delta \bar{\varepsilon}^{pl} = 0$, and

$$\mathbf{F}_{n+1}^p = \mathbf{I} \quad (113)$$

where \mathbf{I} is the second order identity tensor. Then,

$$\mathbf{F}_{n+1}^e = \mathbf{F}_{n+1} \mathbf{F}_{n+1}^{p-1} = \mathbf{F}_{n+1}. \quad (114)$$

Decompose \mathbf{F}_{n+1}^e from Equation 114 into \mathbf{R}_{n+1}^e and \mathbf{U}_{n+1}^e as

$$\mathbf{F}_{n+1}^e = \mathbf{R}_{n+1}^e \mathbf{U}_{n+1}^e. \quad (115)$$

Compute the Hencky strain \mathbf{E}_{n+1}^e as

$$\mathbf{E}_{n+1}^e = \ln(\mathbf{U}_{n+1}^e). \quad (116)$$

Compute the Mandel stress as

$$\mathbf{M}_{n+1}^e = 2G \mathbf{E}_{n+1}^e + K \left[\text{tr}(\mathbf{E}_{n+1}^e) \right] \mathbf{I}. \quad (117)$$

Now Cauchy stress \mathbf{T} can be calculated by transforming the Mandel stress into the current configuration as

$$\mathbf{T}_{n+1} = \frac{1}{J_{n+1}} \mathbf{R}_{n+1}^e \mathbf{M}_{n+1}^e \mathbf{R}_{n+1}^{e\top}. \quad (118)$$

For any time step $n > 0$, assume the following quantities are known from previous step $\{\mathbf{F}_n, \mathbf{F}_n^e, \mathbf{F}_n^p, Y_n, \mathbf{M}_n^e, \bar{\varepsilon}_n^{pl}, h_n\}$. Given \mathbf{F}_{n+1} , our goal is to find $\{\mathbf{F}_{n+1}^e, \mathbf{F}_{n+1}^p, Y_{n+1}, \mathbf{M}_{n+1}^e, \bar{\varepsilon}_{n+1}^{pl}, h_{n+1}\}$. We carry out explicit integration for all the quantities except for the consistency parameter, which we solve through numerical iterations so as to accurately satisfy the consistency condition during yielding. Following steps elaborate the procedure (trial quantities are denoted by **):

Step 1: Compute the volume ratio J_{n+1} using

$$J_{n+1} = \det(\mathbf{F}_{n+1}). \quad (119)$$

Step 2: Compute

$$\mathbf{F}_{n+1}^{e**} = \mathbf{F}_{n+1} \mathbf{F}_n^{p-1}. \quad (120)$$

Step 2.1:

$$\mathbf{F}_{n+1}^{e**} = \mathbf{R}_{n+1}^{e**} \mathbf{U}_{n+1}^{e**}. \quad (121)$$

Step 2.2: Compute the Hencky strain \mathbf{E}_{n+1}^{e**} as

$$\mathbf{E}_{n+1}^{e**} = \ln(\mathbf{U}_{n+1}^{e**}). \quad (122)$$

Step 2.3: Compute the Mandel stress as

$$\mathbf{M}_{n+1}^{e**} = 2G \mathbf{E}_{n+1}^{e**} + K \left[\text{tr}(\mathbf{E}_{n+1}^{e**}) \right] \mathbf{I}. \quad (123)$$

Step 2.4: Compute the equivalent (von mises) stress in the intermediate configuration using the deviatoric part of the Mandel stress:

$$(\sigma_v^{**})_{n+1} = \sqrt{\frac{3}{2}(\mathbf{M}_{n+1}^{e**})_0 : (\mathbf{M}_{n+1}^{e**})_0}. \quad (124)$$

In the above equation $(\mathbf{M}_{n+1}^{e**})_0$ denotes the deviatoric part of the Mandel stress \mathbf{M}_{n+1}^{e**} . $(\mathbf{M}_{n+1}^{e**})_0$ is given by

$$(\mathbf{M}_{n+1}^{e**})_0 = \mathbf{M}_{n+1}^{e**} + \bar{p}_{n+1}^{**} \mathbf{I}, \quad (125)$$

where

$$\bar{p}_{n+1}^{**} = -\frac{1}{3} \text{tr}(\mathbf{M}_{n+1}^{e**}), \quad (126)$$

and \mathbf{I} is the second order identity tensor. Here we have not included any kinematic hardening (or back stress). Mandel stress is work conjugate to the plastic velocity gradient, and we have assumed plastic spin to be zero (on grounds of material isotropy), and plastic velocity gradient is essentially plastic stretching.

Step 3: Now we check for yielding by comparing the equivalent stress $(\sigma_v^{**})_{n+1}$, given by Equation 134, and current yield strength Y_n . If $(\sigma_v^{**})_{n+1} - Y_n < 0$, then the current increment is only elastic, set equivalent plastic strain increment to be zero ($\Delta \varepsilon_n^{pl} = 0$), and goto **Step 6**.

Step 4: If the yield condition is satisfied and plasticity has to occur, then we calculate the direction of plastic flow (\mathbf{N}_n^p) and take it to be co-linear with the deviatoric part of Mandel stress.

$$\mathbf{N}_n^p = \frac{(\mathbf{M}_n^e)_0}{\sqrt{\frac{2}{3}(\mathbf{M}_n^e)_0 : (\mathbf{M}_n^e)_0}}. \quad (127)$$

Step 5: The plastic stretching \mathbf{D}_n^p is given as

$$\mathbf{D}_n^p = \dot{\lambda} \mathbf{N}_n^p, \quad (128)$$

where $\dot{\lambda}$ is the equivalent plastic strain rate. If we assume that the current time step is small then $\dot{\lambda} dt = \Delta \varepsilon_n^{pl} = d\lambda$. Now the goal is to find the incremental equivalent plastic strain such that consistency condition for the yield locus is satisfied.

Step 5: Here we demonstrate how to solve for the consistency parameter ($d\lambda$) through iterations. During this iterative search we use $(**)$ to denote trial quantities. We start with some trial value for consistency parameter as $d\lambda^{**}$.

Step 5.1: Compute trial plastic deformation gradient (recall that in a continuum setting we have $\dot{\mathbf{F}}^p = \mathbf{D}^p \mathbf{F}^p$)

$$\mathbf{F}_{n+1}^{p**} = \mathbf{F}_n^p + d\lambda^{**} \mathbf{N}_n^p \mathbf{F}_n^p. \quad (129)$$

Step 5.2: Compute trial elastic deformation gradient

$$\mathbf{F}_{n+1}^{e**} = \mathbf{F}_{n+1}^p \mathbf{F}_{n+1}^{p*-1}. \quad (130)$$

Step 5.3: Decompose the obtained \mathbf{F}_{n+1}^{e**} from Equation 130 into \mathbf{R}_{n+1}^{e**} and \mathbf{U}_{n+1}^{e**} as

$$\mathbf{F}_{n+1}^{e**} = \mathbf{R}_{n+1}^{e**} \mathbf{U}_{n+1}^{e**}. \quad (131)$$

Step 5.4: Compute the trial Hencky strain \mathbf{E}_{n+1}^{e**} as

$$\mathbf{E}_{n+1}^{e**} = \ln(\mathbf{U}_{n+1}^{e**}). \quad (132)$$

Step 5.5: Compute the trial Mandel stress as

$$\mathbf{M}_{n+1}^{e**} = 2G \mathbf{E}_{n+1}^{e**} + K \left[\text{tr}(\mathbf{E}_{n+1}^{e**}) \right] \mathbf{I}, \quad (133)$$

Step 5.6: Compute the trial equivalent (von Mises) stress in the intermediate configuration using the deviatoric part of the Mandel stress.

$$(\sigma_v)_{n+1}^{**} = \sqrt{\frac{3}{2} (\mathbf{M}_{n+1}^{e**})_0 : (\mathbf{M}_{n+1}^{e**})_0}, \quad (134)$$

where

$$(\mathbf{M}_{n+1}^{e**})_0 = \mathbf{M}_{n+1}^{e**} + \bar{p}_n^{**} \mathbf{I}, \quad (135)$$

and

$$\bar{p}_{n+1}^{**} = -\frac{1}{3} \text{tr}(\mathbf{M}_{n+1}^{e**}). \quad (136)$$

Step 5.7: Compute trial value of the new yield locus:

$$Y_n^{**} = Y_n + h_{n+1}^{**} d\lambda^{**}. \quad (137)$$

In the above h_n^{**} is the hardening modulus (and depends upon the accumulated plastic strain).

Step 5.8: Check whether the consistency condition is satisfied:

$$(\sigma_v)_{n+1}^{**} - Y_n - h_{n+1}^{**} d\lambda^{**} = 0 \quad (138)$$

If the above equation is not satisfied (according to some predefined numerical tolerance), then choose the different value of $d\lambda^{**}$ and go to **Step 5.1**. We performed this iterative procedure using a Bisection method.

Step 5.9: The solution $d\lambda$ satisfying the Equation 138 is taken as the incremental equivalent plastic strain ($\Delta\bar{\varepsilon}_n^{pl}$)

$$\Delta\bar{\varepsilon}_n^{pl} = d\lambda. \quad (139)$$

Also, the value of the hardening modulus satisfying the consistency condition is updated as h_{n+1} .

Step 6: Compute the plastic part of the deformation gradient at time t_{n+1} as

$$\mathbf{F}_{n+1}^p = \mathbf{F}_n^p + \Delta\bar{\varepsilon}_n^{pl} \mathbf{N}_n^p \mathbf{F}_n^p. \quad (140)$$

Step 7: Compute the elastic part of the deformation gradient at time t_{n+1}

$$\mathbf{F}_{n+1}^e = \mathbf{F}_{n+1}^p \mathbf{F}_{n+1}^{p-1}. \quad (141)$$

Step 8: Decompose \mathbf{F}_{n+1}^e from Equation 141 into \mathbf{R}_{n+1}^e and \mathbf{U}_{n+1}^e as

$$\mathbf{F}_{n+1}^e = \mathbf{R}_{n+1}^e \mathbf{U}_{n+1}^e. \quad (142)$$

Step 9: Compute the Hencky strain \mathbf{E}_{n+1}^e as

$$\mathbf{E}_{n+1}^e = \ln(\mathbf{U}_{n+1}^e). \quad (143)$$

Step 10: Compute the Mandel stress at time t_{n+1} as

$$\mathbf{M}_{n+1}^e = 2G\mathbf{E}_{n+1}^e + K \left[\text{tr}(\mathbf{E}_{n+1}^e) \right] \mathbf{I}. \quad (144)$$

Step 10:

Now Cauchy stress \mathbf{T}_{n+1} can be calculated by transforming the Mandel stress into the current configuration as

$$\mathbf{T}_{n+1} = \frac{1}{J_{n+1}} \mathbf{R}_{n+1}^e \mathbf{M}_{n+1}^e \mathbf{R}_{n+1}^{e\top}. \quad (145)$$

Step 11:

Updated yield strength

$$Y_{n+1} = Y_n + h_{n+1} \Delta \bar{\varepsilon}_n^{pl}. \quad (146)$$

Update the total equivalent plastic strain

$$\bar{\varepsilon}_{n+1}^{pl} = \bar{\varepsilon}_n^{pl} + \Delta \bar{\varepsilon}_n^{pl}. \quad (147)$$

3.2 Hypoelasticity: Additive Decomposition of Spatial Strain Rate

In a hypoelastic constitutive law, the time rate change in stress is expressed as some function of time derivatives of strains, and the integration procedure utilized should satisfy the criterion of “incremental objectivity”, see [36, 80]. The stresses are obtained by integration of these rate-type equations, see [78, 27, 96, 67, 48, 95]. Using Equation 11, we can write

$$\mathbf{D} = \frac{1}{2} [\mathbf{L} + \mathbf{L}^\top] = Sym(\mathbf{L}), \quad (148)$$

where Sym yields the symmetric part of the operand. Substituting the expression for \mathbf{L} from Equation 17 in Equation 148, we obtain

$$\mathbf{D} = Sym[\mathbf{L}^e + \mathbf{F}^e (\mathbf{D}^p + \mathbf{W}^p) \mathbf{F}^{e-1}]. \quad (149)$$

By setting plastic spin $\mathbf{W}^p = \mathbf{0}$, substituting $\mathbf{F}^e = \mathbf{R}^e \mathbf{U}^e$, and utilizing $\mathbf{D}^e = Sym[\mathbf{L}^e]$ we can re-write Equation 149 as

$$\mathbf{D} = \mathbf{D}^e + Sym[\mathbf{R}^e \mathbf{U}^e (\mathbf{D}^p) \mathbf{U}^{e-1} \mathbf{R}^{e-1}]. \quad (150)$$

Further if elastic stretches are small, i.e. $\mathbf{U}^e \approx 1$, then above equation can be reduced to

$$\mathbf{D} = \mathbf{D}^e + Sym[\mathbf{R}^e (\mathbf{D}^p) \mathbf{R}^{e-1}]. \quad (151)$$

It can be shown that $\mathbf{R}^e (\mathbf{D}^p) \mathbf{R}^{e-1}$ is symmetric and hence we can re-write

$$\mathbf{D} = \mathbf{D}^e + \bar{\mathbf{D}}^p, \quad (152)$$

with

$$\bar{\mathbf{D}}^p = \mathbf{R}^e \mathbf{D}^p \mathbf{R}^{e-1} = \mathbf{R}^e \mathbf{D}^p \mathbf{R}^{e\top}. \quad (153)$$

Equation 152 is commonly known as the additive decomposition of the spatial strain rate. Material models based on above decomposition of require evolution rule for \mathbf{D}^e and \mathbf{D}^p (or $\bar{\mathbf{D}}^p$). One of the commonly utilized measure of objective rate is known as the Jaumman rate, and the Jaumman rate of cauchy stress (denoted by \mathbf{T}^J) is given as

$$\mathbf{T}^J = \dot{\mathbf{T}} - \mathbf{W}\mathbf{T} + \mathbf{T}\mathbf{W}, \quad (154)$$

where $\dot{\mathbf{T}}$ is the material derivative of the Cauchy stress with respect to undeformed (fixed) basis. \mathbf{T}^J is also known co-rotational stress rate as it corresponds to the time rate of change with respect to the observer-frame attached and rigidly-rotating with the material point of interest. It should be noted that the hypoelastic relation given by Equation 154 is not known to be thermodynamically consistent, in the sense that constitutive equation for \mathbf{T} is not derived from a free energy function, i.e., path independence aspect is missing from its definition. Issues with rate-type formulations have been well-known [89, 47], however, given their simplicity, efficiency, and applicability for problems with small elastic strains they are still practiced [50, 26, 59]. The constitutive equation for *small* strain elasticity is

$$\mathbf{T} = \mathbb{C} : \mathbf{E}^e, \quad (155)$$

where \mathbb{C} is the fourth order elasticity tensor

$$\mathbb{C} = \left(K - \frac{2}{3}G \right) \mathbf{I} \otimes \mathbf{I} + 2G\mathbb{I}. \quad (156)$$

Equation 155 can also be written in a Jaumann (corotational) *rate form* as

$$\mathbf{T}^J = \mathbb{C} : \mathbf{D}^e. \quad (157)$$

This finally reduces to

$$\mathbf{T}^J = \left(K - \frac{2}{3}G \right) (\mathbf{I} : \mathbf{D}^e) \mathbf{I} + 2G\mathbf{D}^e. \quad (158)$$

It should be noted that the above constitutive law describing the elastic deformation satisfies the requirement of “frame-indifference,” or objectivity. Now we need to specify the evolution law for the plastic flow $\bar{\mathbf{D}}^p$. As shown in the previous section, Equation 107 (the normality flow rule) can be used to write

$$\mathbf{D}^p = \dot{\lambda} \mathbf{N}^p = \dot{\lambda} \frac{\mathbf{M}_0^e}{|\mathbf{M}_0^e|}, \quad (159)$$

where $\dot{\lambda}$ is the consistency parameter, and we have used Equation 107 for the direction of plastic flow. From Equation 93, we know that during yielding $|\mathbf{M}_0^e| = Y(e^p)$. In hypoelasticity the relation between Cauchy stress and Mandel stress (Equation 92) can be reduced to (by choosing $\mathbf{U}^e \approx 1$ and $J \approx 1$) as

$$\mathbf{T} = \mathbf{R}^e \mathbf{M}^e \mathbf{R}^{e\top}. \quad (160)$$

Accordingly, it can be shown that $\mathbf{T}_0 = \mathbf{R}^e \mathbf{M}_0^e \mathbf{R}$, and substituting Mandel stress in terms of Cauchy

stress, and $|\mathbf{M}_0^e| = Y(e^p)$ in Equation 159, we can obtain

$$\mathbf{D}^p = \dot{\lambda} \left(\frac{\mathbf{R}^{-e} \mathbf{T}_0 \mathbf{R}^{-e\top}}{Y(e^p)} \right). \quad (161)$$

Using Equation 153, Equation 161 can be re-written as

$$\bar{\mathbf{D}}^p = \dot{\lambda} \left(\frac{\mathbf{T}_0}{Y(e^p)} \right). \quad (162)$$

Thus, we have obtained the flow rule in terms of Cauchy stress. Also, $\dot{\lambda} = \dot{e}^p = |\bar{\mathbf{D}}|$. In case of hypoelasticity, it is easy to show that $|\mathbf{M}_0^e| = |\mathbf{T}_0|$, thus the yield function given in Equation 95 can be re-written as

$$f_h = |\mathbf{T}_0| - Y(e^p), \quad (163)$$

where f_h indicates specialization of the yield function in case of hypoelasticity. Now during plastic yielding ($f_h = 0$ and $\dot{f}_h = 0$), i.e.,

$$\dot{f}_h = \frac{\dot{|\mathbf{T}_0|}}{|\mathbf{T}_0|} - \frac{\dot{Y(e^p)}}{Y(e^p)}, \quad (164)$$

$$\dot{f}_h = \frac{\mathbf{T}_0}{|\mathbf{T}_0|} : \dot{\mathbf{T}}_0 - H(e^p) |\bar{\mathbf{D}}^p|. \quad (165)$$

Now we define the direction of plastic flow in current configuration as

$$\bar{\mathbf{N}}^p = \frac{\mathbf{T}_0}{|\mathbf{T}_0|}, \quad (166)$$

and accordingly re-write the Equation 167 as

$$\dot{f}_h = \bar{\mathbf{N}}^p : \dot{\mathbf{T}}_0 - H(e^p) |\bar{\mathbf{D}}^p|. \quad (167)$$

Since $\bar{\mathbf{N}}^p$ is deviatoric and $\dot{\mathbf{T}}$ is symmetric, therefore $\bar{\mathbf{N}}^p : \dot{\mathbf{T}}_0 = \bar{\mathbf{N}}^p : \dot{\mathbf{T}}$. Thus during active yielding, we have $\bar{\mathbf{D}}^p \neq \mathbf{0}$, and $\dot{f}_h = 0$, therefore Equation 167 becomes

$$\bar{\mathbf{N}}^p : \dot{\mathbf{T}} - H(e^p) |\bar{\mathbf{D}}^p| = 0. \quad (168)$$

From Equation 154, we can substitute $\dot{\mathbf{T}}$ in terms of \mathbf{T}^J , \mathbf{T} and \mathbf{W} , in Equation 168, to finally obtain

$$\bar{\mathbf{N}}^p : \mathbf{T}^J - H(e^p) |\bar{\mathbf{D}}^p| = 0. \quad (169)$$

Equation 157 can be re-written as

$$\mathbf{T}^J = \mathbb{C} : (\mathbf{D} - \bar{\mathbf{D}}^p), \quad (170)$$

and substituting $\bar{\mathbf{D}} = \dot{\lambda} \bar{\mathbf{N}}^p$, we have

$$\mathbf{T}^J = \mathbf{C} : \mathbf{D} - \dot{\lambda} \mathbf{C} : \bar{\mathbf{N}}^p. \quad (171)$$

Substituting \mathbf{T}^J from Equation 171 into Equation 169, and writing $|\bar{\mathbf{D}}^p| = \dot{\lambda}$, we can solve for $\dot{\lambda}$ as

$$\dot{\lambda} = \frac{\bar{\mathbf{N}}^p : \mathbf{C} : \mathbf{D}}{H(e^p) + \bar{\mathbf{N}}^p : \mathbf{C} : \bar{\mathbf{N}}^p}. \quad (172)$$

Finally back substituting $\dot{\lambda}$ from Equation 172 in Equation 171, we obtain

$$\mathbf{T}^J = \mathbf{C} : \mathbf{D} - \frac{\bar{\mathbf{N}}^p : \mathbf{C} : \mathbf{D}}{H(e^p) + \bar{\mathbf{N}}^p : \mathbf{C} : \bar{\mathbf{N}}^p} \mathbf{C} : \bar{\mathbf{N}}^p, \quad (173)$$

and upon rearranging we can rewrite above equation as

$$\mathbf{T}^J = \left(\mathbf{C} - \frac{\mathbf{C} : \bar{\mathbf{N}}^p \otimes \bar{\mathbf{N}}^p : \mathbf{C}}{H(e^p) + \bar{\mathbf{N}}^p : \mathbf{C} : \bar{\mathbf{N}}^p} \right) : \mathbf{D}. \quad (174)$$

Accordingly, the elasto-plastic tangent modulus is given as

$$\mathbf{C}^{ep} = \left(\mathbf{C} - \frac{\mathbf{C} : \bar{\mathbf{N}}^p \otimes \bar{\mathbf{N}}^p : \mathbf{C}}{H(e^p) + \bar{\mathbf{N}}^p : \mathbf{C} : \bar{\mathbf{N}}^p} \right). \quad (175)$$

Equation 175 provides Jaumann stress rate in terms of spatial stretching, and now we need to integrate these equations with respect to time to obtain stresses and other deformation fields.

3.2.1 Time Integration Rate-Independent Hypoelasticity

We again follow a deformation driven problem structure and the computation of strain increment for the co-rotational updates is computed using mid-point rule as proposed by Hughes and Winget [36]²

Initialization: For $n = 0$,

$$\text{Initialize } \mathbf{N}_{n+1}^p = \mathbf{0}, \Delta \bar{\varepsilon}_{n+1}^{pl} = \mathbf{0}, \mathbf{T}_{n+1} = \mathbf{0}, \mathbf{T}_{n+1}^J = \mathbf{0}.$$

At any time $n + 1 > 0$

²We assume that we have the solution to the problem up to time t_n (when \mathbf{x}_n is the spatial location), and at time t_{n+1} the prescribed deformation takes a material element to the spatial point \mathbf{x}_{n+1} . This is equivalent way of saying that solution up to \mathbf{F}_n is known, and we need to find the solution corresponding to \mathbf{F}_{n+1} . We denote the incremental displacement as $\mathbf{u} = \mathbf{x}_{n+1} - \mathbf{x}_n$, and a mid-point configuration $\mathbf{x}_{n+\frac{1}{2}} = \frac{1}{2}(\mathbf{x}_{n+1} + \mathbf{x}_n)$. Now the increment in the strain, from t_n to t_{n+1} , are computed with respect to this mid-point configuration as:

$$\Delta \mathbf{E}_{n+1} = \frac{1}{2} \left(\frac{\partial \mathbf{u}}{\partial \mathbf{x}_{n+\frac{1}{2}}} + \left(\frac{\partial \mathbf{u}}{\partial \mathbf{x}_{n+\frac{1}{2}}} \right)^T \right). \text{ This maintains second order accuracy as long as time steps are } \textit{small}.$$

We assume that quantities at time the beginning of the time increment t_{n+1} (i.e. at the end of t_n) are known: Cauchy stress (\mathbf{T}_n) , co-rotational stress (\mathbf{T}_n^J) , yield strength Y_n , $\bar{\varepsilon}_n^{pl}$, h_n . Now given \mathbf{F}_{n+1} , $\Delta t_{n+1} (= t_{n+1} - t_n)$, the goal is to find the updated quantities as \mathbf{T}_{n+1} , co-rotational stress \mathbf{T}_{n+1}^J , yield strength Y_{n+1} , $\bar{\varepsilon}_{n+1}^{pl}$, h_{n+1} . A radial-return algorithm is used to satisfy the yield condition. In what follows, the trial quantities are denoted **. For a given strain increment $\Delta \mathbf{E}_{n+1}$, the goal is to find the additive split of the strain increment into elastic and plastic parts as

$$\Delta \mathbf{E}_{n+1} = \Delta \mathbf{E}_{n+1}^e + \Delta \mathbf{E}_{n+1}^p \quad (176)$$

Step 1: Compute the trial corrotational stress using the strain increment as

$$\mathbf{T}_{n+1}^{J**} = \mathbf{T}_n^J + (K - \frac{2}{3}G)tr(\Delta \mathbf{E}_{n+1}) + 2G\Delta(\mathbf{E}_{n+1})_0. \quad (177)$$

Step 2: Compute the trial equivalent von-mises stress

$$(\sigma_v)_{n+1}^{**} = \sqrt{\frac{3}{2}(\mathbf{T}_{n+1}^{J**})_0 : (\mathbf{T}_{n+1}^{J**})_0}. \quad (178)$$

Step 3: If $(\sigma_v)_{n+1}^{**}$ computed in Equation 178 is less than Y_n then it is an elastic increment, set $\Delta \mathbf{E}_{n+1}^p = 0$, and go to Step 4.5, else continue with following.

Step 4: Radial return algorithm is employed to compute the incremental plastic strain. Following steps describe how this is achieved.

Step 4.1: The direction of plastic flow is computed as

$$\mathbf{N}_{n+1}^p = \frac{(\mathbf{T}_{n+1}^{J**})_0}{\sqrt{\frac{2}{3}(\mathbf{T}_{n+1}^{J**})_0 : (\mathbf{T}_{n+1}^{J**})_0}}. \quad (179)$$

Step 4.2: The magnitude of the incremental equivalent plastic strain $(\Delta \bar{\varepsilon}^{pl})$ is obtained by consistently linearizing and satisfying the yield condition, which yields

$$(\Delta \bar{\varepsilon}^{pl})_{n+1} = \frac{(\sigma_v)_{n+1}^{**} - Y_n}{3\mu + h_n}. \quad (180)$$

Step 4.3: The incremental plastic strain is obtained as

$$\Delta \mathbf{E}_{n+1}^p = \Delta \bar{\varepsilon}_{n+1}^{pl} \mathbf{N}_{n+1}^p. \quad (181)$$

Step 4.4: By using Equation 180, the yield strength at t_{n+1} is updated as

$$Y_{n+1} = Y_n + h_n \times (\Delta \bar{\varepsilon}^{pl})_{n+1} \quad (182)$$

The hardening modulus is also updated in accordance with the experimental data.

Step 4.5: Compute the elastic strain by subtracting the plastic strain increment given by Equation 181 from the total strain increment as

$$\Delta \mathbf{E}_{n+1}^e = \Delta \mathbf{E}_{n+1} - \Delta \mathbf{E}_{n+1}^p. \quad (183)$$

Step 5: Compute the updated corrotational stress using the incremental elastic strains from Equation 183.

$$\mathbf{T}_{n+1}^J = \mathbf{T}_n^J + \left(K - \frac{2}{3}G \right) tr(\Delta \mathbf{E}_{n+1}^e) + 2G(\Delta \mathbf{E}_{n+1}^e)_0 \quad (184)$$

Step 6: Obtain the Cauchy stress by transforming the corrotational stress into the current frame as

$$\mathbf{T}_{n+1} = \mathbf{R}_{n+1} \mathbf{T}_{n+1}^J \mathbf{R}_{n+1}^T, \quad (185)$$

where \mathbf{R}_{n+1} is obtained from polar decomposition of \mathbf{F}_{n+1} as

$$\mathbf{F}_{n+1} = \mathbf{R}_{n+1} \mathbf{U}_{n+1}. \quad (186)$$

3.3 Solution to Global Equilibrium Equations Using Abaqus Explicit Dynamics

The Explicit dynamicS solver used by Abaqus is based on the central difference formulas for the velocity and the acceleration, and the use of diagonal or lumped element mass matrices is adopted. The quantities such as displacement, velocities and accelerations are specified at nodal points. Let \mathcal{F}_n and \mathcal{I}_n denote the external and internal (due to resultant of internal stresses) nodal point force vectors³. Then nodal point acceleration vector ($\ddot{\mathcal{U}}_n$) is given as

$$\ddot{\mathcal{U}}_n = \mathcal{M}^{-1}(\mathcal{F}_n - \mathcal{I}_n), \quad (187)$$

where \mathcal{M} is the diagonal lumped mass matrix. \mathcal{I} is obtained from the VUMAT implementation of the material model. The nodal velocity vector, at mid-point time, is then computed as

$$\dot{\mathcal{U}}_{n+\frac{1}{2}} = \dot{\mathcal{U}}_{n-\frac{1}{2}} + \frac{\Delta t_{n+\frac{1}{2}} + \Delta t_n}{2} \ddot{\mathcal{U}}_n, \quad (188)$$

and the updated nodal point displacement vector is then computed as

$$\mathcal{U}_{n+1} = \mathcal{U}_n + \Delta t_{n+1} \dot{\mathcal{U}}_{n+\frac{1}{2}}. \quad (189)$$

³Nodal values are interpolated at the Gauss integration points of the element via shape functions of the used element. Obtained interpolated quantities at integration points are passed either to VUMAT or Abaqus material library to obtain stresses at the integration points which are further integrated for the whole element. This integrated stresses for the element is the internal force \mathcal{I} which is assembled for all the elements.

where Δt is defined as

$$\Delta t_{n+1} = t_{n+\frac{1}{2}} - t_{n-\frac{1}{2}}. \quad (190)$$

As stated earlier, the explicit procedure does not require any tangent stiffness, and for quasi-static problems (where acceleration terms are negligible) the \mathcal{M} matrix can be scaled. However, caution must be taken that mass scaling does not lead to excessively high and unrealistic kinetic energies.

3.4 Contact Interaction and Friction

We employed the default kinematic constraint algorithm for the contact interaction. In particular, the tangential behavior was modeled through a penalty formulation (with a very large penalty factor of 10^{10}), and in absence of slip the relative tangential displacement is computed by dividing the frictional force by the chosen penalty factor. Such an approach is helpful when friction can cause excessive local distortion. The contact algorithm in a pure master-slave surface formulation, detects contact when the slave node penetrates into the master segment, therefore a sufficiently fine mesh for both bodies are chosen so that no spurious interpenetrations of the rigid-roller into the ductile film substrate occur. Additionally, large roller radii, slow angular speeds, and sufficiently fine mesh enable robust performance of the contact algorithm. Although not necessarily required, we chose to work with a finite sliding formulation, i.e., detect a change in master segment for every slave node (through a global search) after a set number of time increments. For the sake of completeness, a summary of the contact algorithm for rigid (master) and soft surface (slave) is given in Algorithm 1.

4 Experimental and Simulation Results

Material calibration: Uniaxial tensile tests were carried out on polymer films at a strain rate of 0.0025 sec^{-1} . The yield strength and elastic modulus of the films were found to be $\sigma_{y, film} = 4 \text{ MPa}$ and $E_{film} = 78 \text{ MPa}$, respectively. Accordingly, the elastic limit, $\epsilon_e = \sigma_{y, film} / E_{film}$, was estimated as 5% strain, which is a major contrast with respect to rigid-plastic model. The elastic modulus, yield strength, and hardening data were used to calibrate hypoelastic and multiplicative plasticity models. The performance of the multiplicative plasticity based model and hypoelastic formulation, calibrated against tensile test, is shown in Figure 8. It is clear polymer films have noticeable elastic range, and harden with increasing plastic deformation. As will become clear, such type of material behavior (which is quite distinct from metals) is not accounted in classical rolling theories, and therefore an appropriate finite element model is required for polymer rolling. The calibrated material models were used in rolling simulations.

Algorithm 1 Pseudo code for Abaqus/Explicit Contact for rigid (master) segment and soft (slave) node interaction. Assumed that master surface follows a displacement specified motion.

```

1: procedure CONTACT
2:   Time  $\rightarrow t_n$                                  $\triangleright$  All quantities known, need to find explicit updates from  $t_n$  to  $t_{n+1}$ 
3:    $\mathbf{S}^{t_{n+1}}$                                  $\triangleright$  Perform trial kinematic update of the slave node
4:    $\mathbf{M}^{t_{n+1}}$                                  $\triangleright$  Perform the kinematic update of the current master segment
5:   if (no penetration) then                     $\triangleright$  Check penetration of slave node into the current master segment
6:     return false;                                 $\triangleright$  No contact and proceed to the next slave node
7:   else                                           $\triangleright$  There is penetration and corrector phase starts
8:      $\mathbf{N}^{t_n}$                                  $\triangleright$  Calculate normal to the current master segment
9:      $\boldsymbol{\tau}^{t_n}$                            $\triangleright$  Calculate tangent to the current master segment
10:     $\mathbf{RP}^{t_n}$                                  $\triangleright$  Calculate nearest point on the master segment w.r.t. slave node at  $t_n$ 
11:     $\mathbf{RP}^{t_{n+1}}$                              $\triangleright$  Calculate position of  $\mathbf{RP}^{t_n}$  at time  $t_{n+1}$  on the master segment
12:     $+\mathbf{S}^{t_{n+1}}$                              $\triangleright$  Project slave node from position  $\mathbf{S}^{t_{n+1}}$  along  $\mathbf{N}^{t_n}$ 
13:     $\mathbf{F}_N^{t_n}$                                  $\triangleright$  Solve equation of motions to find normal force needed to prevent interpenetration
14:    if (no friction) then                     $\triangleright$  Check if friction is specified for the problem
15:      return false;                                 $\triangleright$  No tangential force and proceed for the next slave node
16:    else                                           $\triangleright$  Friction is specified
17:       $\delta U$                                  $\triangleright$  Compute relative displacement in tangential direction
18:      if ( $|\delta U| > 0$ ) then                     $\triangleright$  Slip will occur
19:         $\mathbf{F}_{fr}^{t_n}$                              $\triangleright$  Compute tangential force  $\mathbf{F}_{fr}^{t_n}$  assuming no slip
20:        if ( $\mathbf{F}_{fr}^{t_n} > \mu \mathbf{F}_N^{t_n}$ ) then     $\triangleright$  Slip will occur
21:           $++\mathbf{S}^{t_{n+1}} \leftarrow +\mathbf{S}^{t_{n+1}}$      $\triangleright$  Update the projected location of the slave node
22:           $\mathbf{F}_{fr}^{t_n} \leftarrow \mu \mathbf{F}_N^{t_n}$      $\triangleright$  Maximum value of  $\mathbf{F}_{fr}^{t_n}$  can be  $\mu \mathbf{F}_N^{t_n}$ 
23:        else
24:          return false;                             $\triangleright$  No slip (if penalty formulation compute small tangential motion)
25:        else                                           $\triangleright$  No relative displacement
26:          return false;                             $\triangleright$  No tangential force and proceed for the next slave node
27:     $t_n \leftarrow t_{n+1}$                          $\triangleright$  Update time
28:    If specified, update master segment for the slave node     $\triangleright$  At the end of time increment

```

Frictional interaction: We will treat the incoming stack of films as a single sheet under the assumption that there is no relative slippage between them, and will verify this assumption. To model the interaction between the stainless steel rollers and the film stack with Coulombic friction, we need to estimate the coefficient of friction. For this purpose, the coefficient of friction between a stainless steel block (made of same material and surface properties as the rollers), and polymer films was estimated using a friction-fixture on Instron mechanical tester [1]. Stainless steel block of approximately 500 g was used, and the load vs. displacement during sliding motion of the block on the film was recorded, shown in Figure 9. The coefficient of friction μ was estimated to be 0.4. In the finite element simulations we used the isotropic Coulomb friction model, with coefficient of friction of 0.4, and limited the maximum value of the shear-traction equal to the shear yield strength of the material. The Coulombic friction model is schematically shown in Figure 10, where tangential traction is dependent on the normal traction but limited by the material's yield strength.

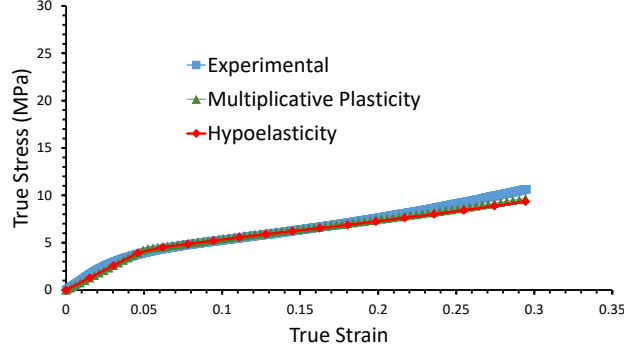


Figure 8: Comparison of true stress-true strain curves based on experimental data, hypoelastic formulation, and $\mathbf{F}^e\mathbf{F}^p$ based decomposition. For both hypoelastic and $\mathbf{F}^e\mathbf{F}^p$ based computation, a rate-independent and isotropic hardening deformation model was employed.

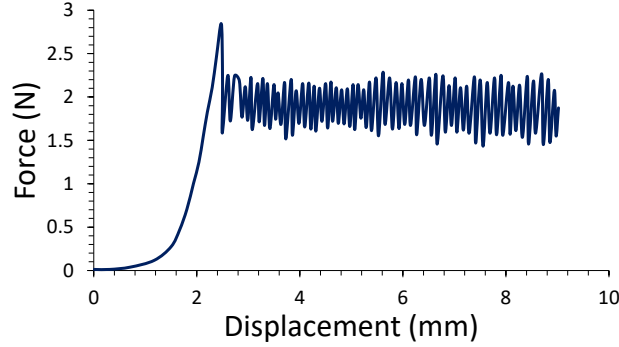


Figure 9: Force versus displacement curve during measurement of coefficient of friction on Instron mechanical tester. The coefficient of friction is estimated from the average force ($F_{friction}$), in the steady state sliding, as $\mu = F_{friction}/m'g$, where $m'g$ is the weight of the block. For $m' = 0.5$ kg and $F_{friction} = 2$ N (based on this graph), μ_k is estimated to be 0.4.

Rolling experiments: A snapshot of the roll-bonding is shown in Figure 3, where multiple layers are fed through the rollers. Several specimens comprising of a film-stack were rolled at different levels of compression loads, leading to different levels of plastic strain. The initial widths of specimens (which were approximately 15 mm) before rolling, were found to be measurably unchanged after rolling, and therefore rolling passes were consistent with the plane-strain scenario. The initial thickness of film-stacks were approximately 0.6 mm, and the average final thickness of the rolled stock depended on the level of plastic-strain imposed. For a detailed correlation between imposed plastic strain and degree of bonding see [73, 70].

Rolling simulations: Plane strain rolling simulations were carried out in Abaqus Explicit to study the deformation of polymer films in the roller-bite. A film-stack of initial thickness 0.6 mm was modeled with

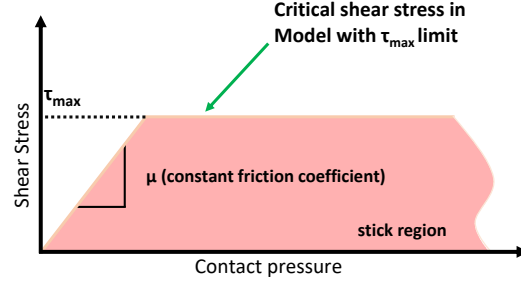


Figure 10: Rate-independent Coulombic friction model).

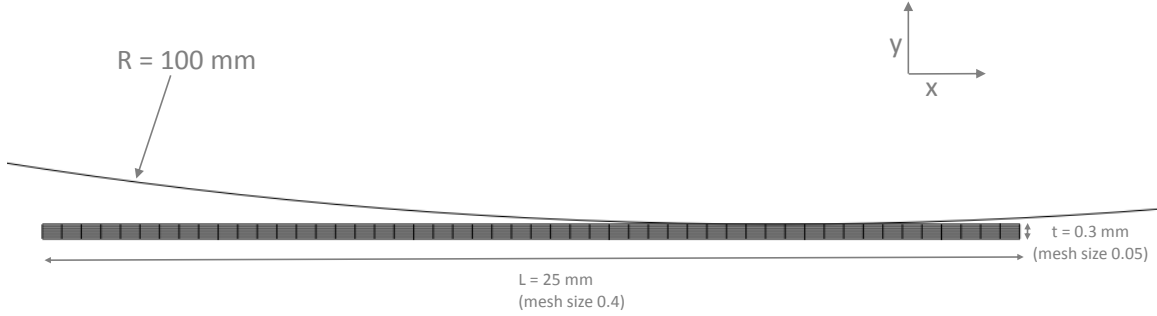


Figure 11: The undeformed mesh in elastic-plastic rolling, only one-half of the model is considered while utilizing symmetry about the XZ symmetry plane.

four-noded plane strain elements with reduced integration (CPE4R), and rollers were treated as rigid surfaces. We utilized the symmetry in rolling, and therefore constructed the simulation model for only one-half of the rolling process, as shown in Figure 11. Mechanical properties of the film, and coefficient of friction between the stack and rollers were used as stated earlier. The incoming films were modeled as a single stack, because the incoming stack had a very small thickness compared to the radius of the rollers (due to which it was expected that there will be negligible shearing through the thickness of the stack, and no slipping or sliding between the film layers). The turning rollers were brought closer, with films in-between them, and the desired level of plastic strains were imposed. Each rolling simulation was continued until rolling loads reached a steady-state value.

Rolling loads based on experiments, rigid-plastic analysis, and elasto-plastic finite element analysis (both, hypoelastic and multiplicative decomposition formulation) are shown in Figure 12. The assumption of rigid-perfectly plastic model, assuming a constant yield stress, is found to greatly underestimate the experimental rolling loads for a desired level of plastic strain, whereas elasto-plastic finite element simulations exhibit an excellent match. Figures 13 and 14, show the plots of von Mises stresses and equivalent plastic strain, for a scenario in which approximately 13.5% nominal thickness reduction was achieved. Clearly, the plots indicate through-thickness and almost homogeneous plastic deformation. The corresponding plots of nominal strain and plastic strain in thickness reduction direction are also shown in Figures 15 and 16, respectively.

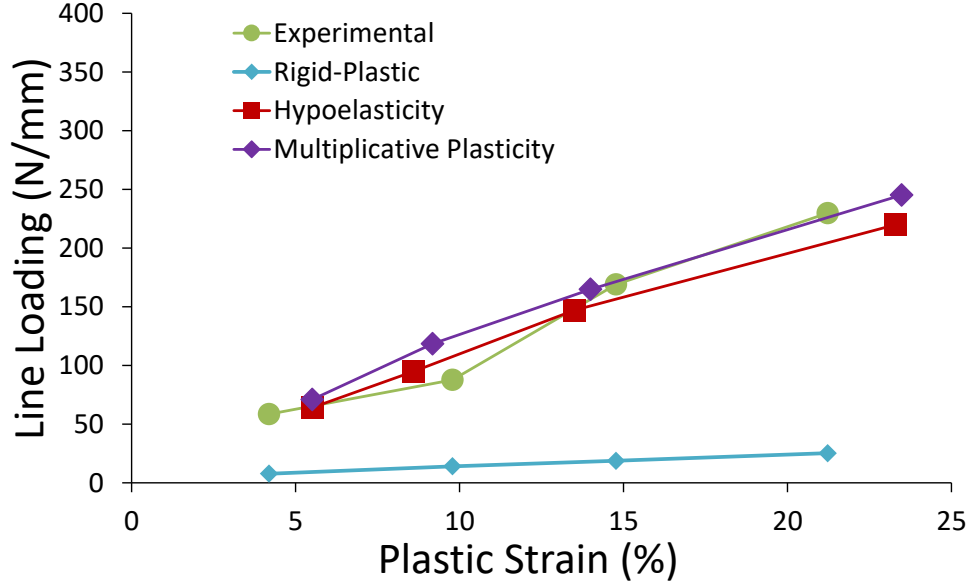


Figure 12: Line loading (N/mm) with respect to % plastic strain curves based on experimental data, and predictions from rigid-perfectly plastic model, and finite strain elastic plastic FEA analysis (both hypoelasticity and multiplicative plasticity).

Since we treated the incoming stack of films as a single strip, to verify our no-slip assumption between the film layers, we plotted the variation of normal stresses and shear stresses along the rolling direction, at the roller-film interface, where the shear stresses attain maximum values (and shear stresses go to zero as the symmetry plane is approached). The variation of shear stresses and normal tractions between roller and film interface is shown in Figure 17. The shear stresses are found to be significantly lower than the normal stresses, and much lower than the shear yield strength of the material. This quantitative data validates the assumption of treating incoming stack of film layers as a single strip, and that an incoming material element deforms homogeneously under normal compression without shearing with respect to the axes of the reference configuration. Furthermore, during rolling and active plastic deformation, as bonding occurs in the rolling bite, the resistance against slipping or sliding will only increase.

To compare the overall accuracy of our explicit dynamics simulations for approximating the quasi-static rolling process, we also compared the plots of total energy of the system, and kinetic energy for the whole model, as function of the simulation time. Total energy should ideally remain constant. Initially the kinetic energy of the model, and total energy, are both zero, and their magnitudes after *long* times, when steady states have been reached, should also be close to zero. The plots of the total energy and kinetic energy, normalized with respect to strain energy, are shown in Figure 19, and are small. These are not exactly zero owing to intrinsic numerical errors during the explicit time integration. The overall excellent energy behavior suggests that explicit integration scheme based on central difference (using automatic time increments), and kinematic constraint algorithm are working accurately over long times.

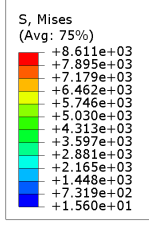


Figure 13: Von Mises stresses during elastic-plastic rolling at steady state for approximately 13.5% nominal strain. The peak S, Mises is 8.611 MPa.

Loss of energy during contact/impact in dynamic problems can be significant [15, 85], but for our rolling cases the material velocities are negligible and therefore concerns related to dissipation during contact, or explicit integration over long times do raise any concern.

The classical model of plastic rolling of a strip is valid when the incoming strip is passed through rollers to produce appreciable reduction in thickness, and when elastic deformations (if any) are negligible compared to plastic strains. This assumption of totally ignoring elastic strains, is often well-suited for metals, since elastic strains typically amount to only 0.5% or so. However, solid state polymers can exhibit elastic strains up to (or greater than) 5% and, therefore such an idealization is expected to yield unsatisfactory results for polymer rolling. In the rigid-plastic model, the maximum nominal strain in thickness is observed at the location where the roller-gap is minimum, and the compression zone spans the region between the the point where the stack first encounters the roller bite and the minimum roller-gap location. In contrast, if the material has sufficient elasticity then for the same level of nominal plastic thickness reduction, the contact zone is much larger on the entry side, and also extends beyond the minimum roller-gap location on the exit side. For the rolling case discussed, where a nominal plastic strain of 13.5% is achieved, we plotted the normalized contact pressure based on the finite element simulation and rigid-plastic model, shown in Figure 17. The minimum rolling gap location is at $x = 0$. Clearly the contact zone and normalized contact pressure for elasto-plastic analysis are significantly larger then the rigid-plastic scheme. This is the primary reason for large polymer rolling loads encountered, which cannot be captured by the classical rolling theories. Such aspects of rolling mechanics are necessarily relevant if polymer films, as those exhibiting hyper-elasticity and plasticity, are to be roll-bonded in a similar fashion.

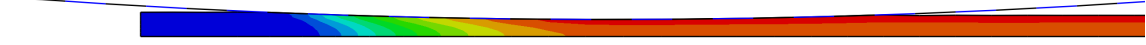
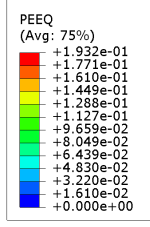


Figure 14: Equivalent plastic strain (PEEQ) during elastic-plastic rolling at steady state for approximately 13.5% nominal strain.

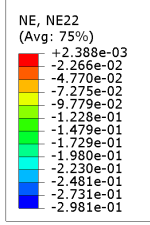


Figure 15: Nominal strain (NE22) in the direction of thickness reduction during elastic-plastic rolling at steady state for approximately 13.5% nominal strain.

5 Equivalency between hypoelasticity and multiplicative decomposition of deformation gradient formulations

In Section 3.2, we showed that hypoelastic formulation and associated additive decomposition of elastic and plastic spatial strain rates can be derived from $\mathbf{F}^e \mathbf{F}^p$ formulation under the assumptions of small elastic stretches, i.e., $\mathbf{U}^e \approx \mathbf{I}$. However, for moderately large rolling strains, the elastic stretches are non-negligible, and the hypoelastic formulation is still found to yield satisfactory performance. This behavior can be understood by noting that even though elastic stretches are moderately large, the rotation tensors for material elements during rolling are close to identity when stack thicknesses are very small compared to the roller radii. Consider Equation 150, where the spatial strain rate for $\mathbf{F}^e \mathbf{F}^p$ formulation is given as

$$\mathbf{D} = \mathbf{D}^e + \text{Sym}[\mathbf{R}^e \mathbf{U}^e (\mathbf{D}^p) \mathbf{U}^{e-1} \mathbf{R}^{e-1}],$$

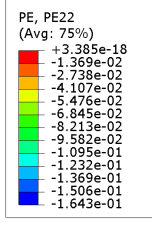


Figure 16: Plastic strain (PE22) in direction of thickness reduction during elastic-plastic rolling at steady state for approximately 13.5% nominal strain.

now if we approximate, both, \mathbf{R}^e and \mathbf{R}^p equal to \mathbf{I} , and assume that material undergoes homogeneous plane strain compression such that \mathbf{U}^e , \mathbf{U}^p , \mathbf{D}^e and \mathbf{D}^p are diagonal, then

$$\mathbf{D} = \mathbf{D}^e + \text{Sym}[\mathbf{U}^e(\mathbf{D}^p)\mathbf{U}^{e-1}]. \quad (191)$$

Accordingly $\mathbf{U}^e(\mathbf{D}^p)\mathbf{U}^{e-1}$ is now symmetric, then Equation 191 reduces to

$$\mathbf{D} = \mathbf{D}^e + \mathbf{U}^e(\mathbf{D}^p)\mathbf{U}^{e-1}, \quad (192)$$

or

$$\mathbf{D} = \mathbf{D}^e + \mathbf{D}^p, \quad (193)$$

where we have used the fact that $\mathbf{U}^e(\mathbf{D}^p)\mathbf{U}^{e-1} = \mathbf{D}^p$, when \mathbf{U}^e and \mathbf{D}^p are diagonal. Equation 193 is the additive decomposition of spatial strain-rate, and same as Equation 152 when elastic rotations are identity. We take note of the fact that although we have assumed plastic spin to be zero, in general that does not imply that plastic part of rotation tensor \mathbf{R}^p is identity, or even constant. In the present rolling scenarios, the geometry and mechanics of deformation, yield all rotation tensors close to identity. Secondly, in the hypoelastic formulation of Section 3.2, we constitutively related the objective stress-rate with elastic stretching Equation 157, and in $\mathbf{F}^e\mathbf{F}^p$ formulation we constitutively related Mandel stress to Hencky strain, and then Cauchy stress with Mandel stress, Equations 91 and 92, respectively. Clearly, in Equation 92 the Mandel stress is equal to Cauchy stress under identity elastic rotation tensors but for a factor of J (capturing volume change between elastically and plastically deformed states), whereas in hypoelasticity the Cauchy stress relates to Hencky strain according to Equation 155 without accounting for such volume changes between incremental elastic and plastic deformations. These differences also explain the small differences between loads predicted by hypoelastic and $\mathbf{F}^e\mathbf{F}^p$ formulation.

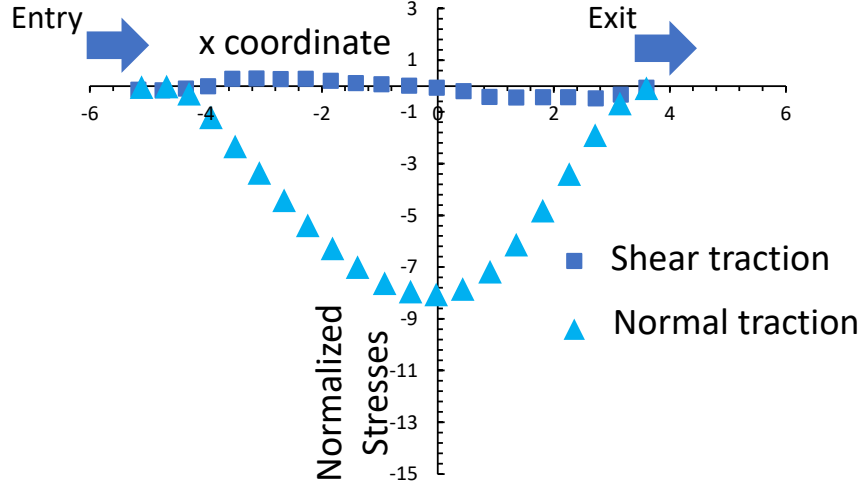


Figure 17: Variation of normalized shear and normal stresses with respect to rolling direction, at steady state for approximately 13.5% nominal strain, between the roller and the film surface. The stresses have been normalized with respect to the yield strength of the films ($\sigma_{y, film}$). The shear stresses are maximum between the roller and the film interface, and zero on the symmetry plane in the thickness direction. The normal stresses were found to be almost uniform across the stock thickness.

6 Conclusions

Cold roll-bonding of polymeric films is a new process, which requires through-thickness and homogeneous plastic deformation of the incoming material strip. In this paper, we have proposed a computationally efficient material modeling approach to carry out cold-rolling finite element simulations. Although analyses of rolling processes have been extensively carried out over last several decades, majority of the classical efforts have focused on applications related to metal deformation, where rigid-perfectly plastic type models are applicable. The distinction between the polymer rolling vs metal rolling is that the polymers can exhibit large elastic stretches, which are completely ignored in the classical rolling theories, and therefore the classical rolling theories cannot be used for making accurate predictions of rolling loads for polymers in general. We noted that in case of polymer rolling, the contact-width and contact-pressure in the roller bite, comprising both elastic and elastic-plastic regions, are substantially larger than those predicted by the rigid-plastic rolling scheme. Finite element simulations, taking elastic deformations into account, up to 20% thickness reductions, give an accurate prediction of the actual rolling loads. While a sophisticated polymer model, with hyperelastic and visco-plastic effects, can be chosen in polymer rolling, we exploited the fact that at low strain-rates and temperatures well-below T_g the polymers do not exhibit rate-sensitivity, thereby allowing us to work with a rate-independent material model which is computationally much faster than simulating a rolling process with rate-dependent effects. Both, rate-independent hypoelastic and multiplicative decomposition, yielded similar predictions and compared well against the experimentally observed loads. In principle, advanced polymer models can also be calibrated

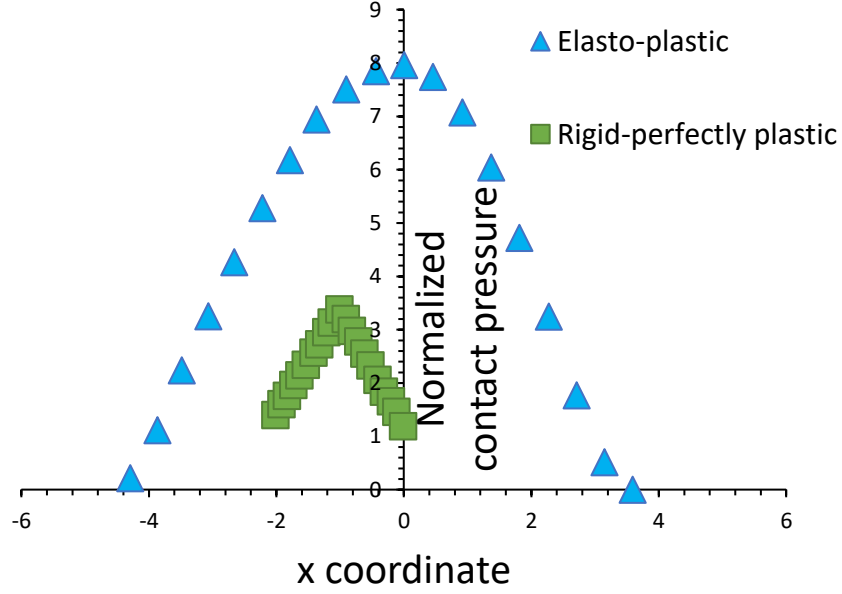


Figure 18: Variation of contact pressure in the roller bite for 13.5% nominal strain based on elasto-plastic finite deformation in ABAQUS and rigid-perfect-plastic model. The contact pressure has been normalized by yield strength of the material.

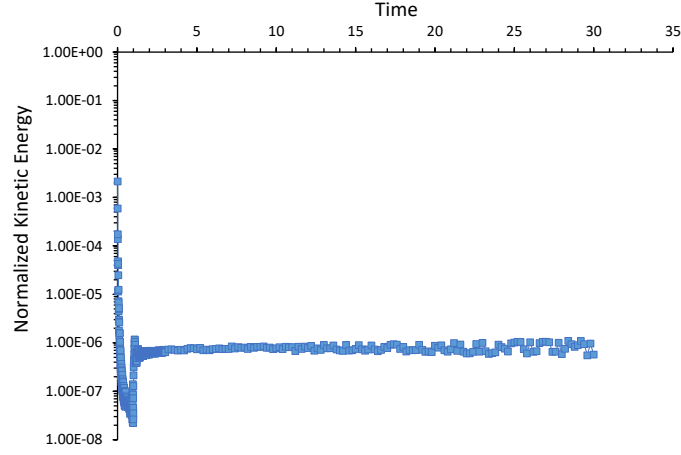
and applied, however, the computational cost involved in various steps during the time-integration of these sophisticated material-models can be significant, without any foreseeable benefits in predictive capability, especially when we are interested in long-time steady-state rolling. An analysis was presented which revealed that hypoelastic material model (which is usually valid for small elastic stretches) is applicable to moderately large elastic stretches, as encountered in rolling of polymers in this study, when principle axes of deformation show negligible rotation (due to large roller radii compared to film thickness). Under such circumstances using a hypoelastic model can also be considered as a more efficient approach compared to $\mathbf{F}^e \mathbf{F}^p$ formulation. We also found that modeling frictional interaction through a rate-dependent Coulombic law, consistent with the rate-independent material model, gave satisfactory results in the rolling simulations.

7 Acknowledgments

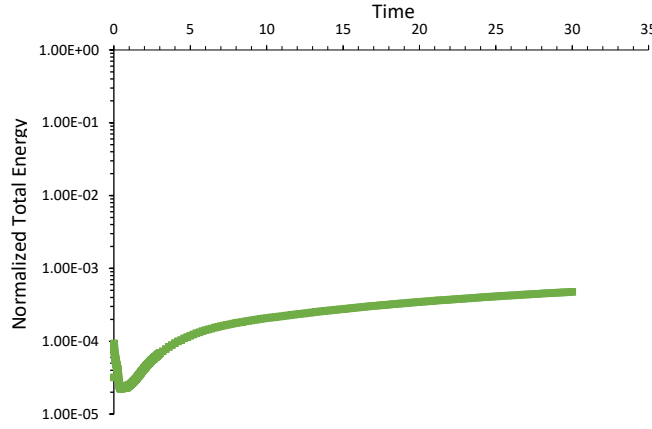
Nikhil Padhye gratefully thanks David Parks for pointing out that rate-independent elasto-plastic analysis could suffice for modeling the plane-strain rolling at low temperatures and strain-rates.

References

- [1] <http://www.instron.com/en-us/products/testing-accessories/grips/application-specific-accessories/friction/2810-005>.



(a) Normalized kinetic energy of finite element model.



(b) Normalized total energy of finite element model.

Figure 19: Normalization of energies has been done with respect to the strain energy of the model at any given time. Both kinetic energy and total energy were initially zero and after *long* time when steady-state has been reached they are still orders of magnitude smaller compared to the dominant strain energy in the model.

- [2] AL-SALEHI, F., FIRBANK, T., AND LANCASTER, P. An experimental determination of the roll pressure distributions in cold rolling. *International Journal of Mechanical Sciences* 15, 9 (1973), 693–710.
- [3] ALEXANDER, J. A slip line field for the hot rolling process. *Proceedings of the Institution of Mechanical Engineers* 169, 1 (1955), 1021–1030.
- [4] ALEXANDER, J., AND FORD, H. Simplified hot-rolling calculations. *Journal of the Institute of Metals* 92 (1964), 397–404.
- [5] AMES, N. M., SRIVASTAVA, V., CHESTER, S. A., AND ANAND, L. A thermo-mechanically coupled theory for large deformations of amorphous polymers. part ii: Applications. *International Journal of Plasticity* 25, 8 (2009), 1495–1539.

- [6] ANAND, L., AND GURTIN, M. E. A theory of amorphous solids undergoing large deformations, with application to polymeric glasses. *International Journal of Solids and Structures* 40, 6 (2003), 1465–1487.
- [7] ARGON, A. S. *The physics of deformation and fracture of polymers*. Cambridge University Press, 2013.
- [8] ARRUDA, E. M., BOYCE, M. C., AND JAYACHANDRAN, R. Effects of strain rate, temperature and thermomechanical coupling on the finite strain deformation of glassy polymers. *Mechanics of Materials* 19, 2 (1995), 193–212.
- [9] AVITZUR, B. An upper-bound approach to cold-strip rolling. *Journal of Manufacturing Science and Engineering* 86, 1 (1964), 31–45.
- [10] BLAND, D., AND FORD, H. The calculation of roll force and torque in cold strip rolling with tensions. *Proceedings of the Institution of Mechanical Engineers* 159, 1 (1948), 144–163.
- [11] BOYCE, M. C., PARKS, D. M., AND ARGON, A. S. Large inelastic deformation of glassy polymers. part i: rate dependent constitutive model. *Mechanics of Materials* 7, 1 (1988), 15–33.
- [12] BROUTMAN, L., AND KRISHNAKUMAR, S. Cold-rolling of polymer: 4. toughness enhancement in amorphous polymers. *Polymer Engineering & Science* 14, 12 (1974), 823–826.
- [13] BROUTMAN, L. J., AND PATIL, R. Cold rolling of polymers. 1 influence of rolling on properties of amorphous polymer. *Polymer Engineering & Science* 11, 2 (1971), 165–173.
- [14] CANGIALOSI, D., WÜBBENHORST, M., SCHUT, H., VAN VEEN, A., AND PICKEN, S. Amorphous-amorphous transition in glassy polymers subjected to cold rolling studied by means of positron annihilation lifetime spectroscopy. *The Journal of chemical physics* 122, 6 (2005), 064702.
- [15] CIRAK, F., AND WEST, M. Decomposition contact response (dcr) for explicit finite element dynamics. *International Journal for Numerical Methods in Engineering* 64, 8 (2005), 1078–1110.
- [16] COLEMAN, B. D., AND NOLL, W. The thermodynamics of elastic materials with heat conduction and viscosity. *Archive for Rational Mechanics and Analysis* 13, 1 (1963), 167–178.
- [17] CORNFIELD, G., AND JOHNSON, R. Theoretical predictions of plastic flow in hot rolling including the effect of various temperature distributions. *Math. Process Models in Iron- and Steelmaking, Metals Society, London. 1975, 280-288, 334-341* (1975).
- [18] COULES, H., COLEGROVE, P., COZZOLINO, L., WEN, S., GANGULY, S., AND PIRLING, T. Effect of high pressure rolling on weld-induced residual stresses. *Science and Technology of Welding and Joining* 17, 5 (2012), 394–401.
- [19] CRANE, F., AND ALEXANDER, J. Slip-line fields and deformation in hot rolling of strip. *Journal of the Institute of Metals* 96, 10 (1968), 289–300.

- [20] DAWSON, P. R. Viscoplastic finite element analysis of steady-state forming processes including strain history and stress flux dependence. Tech. rep., Sandia Labs., Albuquerque, NM (USA), 1978.
- [21] DENTON, B., AND CRANE, F. Roll load and torque in the hot rolling of steel strip. *J IRON STEEL INST* 210, 8 (1972), 606–617.
- [22] DIXIT, P. M., AND DIXIT, U. S. *Modeling of metal forming and machining processes: by finite element and soft computing methods*. Springer Science & Business Media, 2008.
- [23] DIXIT, U., AND DIXIT, P. A finite element analysis of flat rolling and application of fuzzy set theory. *International Journal of Machine Tools and Manufacture* 36, 8 (1996), 947–969.
- [24] DIXIT, U., AND DIXIT, P. Finite-element analysis of flat rolling with inclusion of anisotropy. *International journal of mechanical sciences* 39, 11 (1997), 1237–1255.
- [25] EKELEND, S. *Analysis of Factors Influencing Rolling Pressure and Power Consumption in the Hot Rolling of Steel*. 1933.
- [26] FISH, J., AND SHEK, K. Computational aspects of incrementally objective algorithms for large deformation plasticity. *International Journal for numerical methods in engineering* 44, 6 (1999), 839–851.
- [27] FLANAGAN, D., AND TAYLOR, L. An accurate numerical algorithm for stress integration with finite rotations. *Computer methods in applied mechanics and engineering* 62, 3 (1987), 305–320.
- [28] FORD, H. Researches into the deformation of metals by cold rolling. *Proceedings of the Institution of Mechanical Engineers* 159, 1 (1948), 115–143.
- [29] FORD, H. The theory of rolling. *Metallurgical Reviews* 2, 1 (1957), 1–28.
- [30] GINZBURG, V. B., AND BALLAS, R. *Flat rolling fundamentals*. CRC Press, 2000.
- [31] GOVINDARAJ, N. V., LAUVDAL, S., AND HOLMEDAL, B. Tensile bond strength of cold roll bonded aluminium sheets. *Journal of Materials Processing Technology* 213, 6 (2013), 955–960.
- [32] GRANCIO, M. Cold rolled abs. part 1: The effect of rubber particle size on the tensile properties of abs before and after cold rolling. *Polymer Engineering & Science* 12, 3 (1972), 213–218.
- [33] GURTIN, M. E., FRIED, E., AND ANAND, L. *The mechanics and thermodynamics of continua*. Cambridge University Press, 2010.
- [34] HENNINGSEN, P., ARENTOFT, M., AND WANHEIM, T. Measurements of normal and frictional forces in a rolling process. *Proceedings of the Institution of Mechanical Engineers, Part B: Journal of Engineering Manufacture* 220, 1 (2006), 59–64.
- [35] HIBBITT, H. D., MARCAL, P. V., AND RICE, J. R. A finite element formulation for problems of large strain and large displacement. *International Journal of Solids and Structures* 6, 8 (1970), 1069–1086.

- [36] HUGHES, T. J., AND WINGET, J. Finite rotation effects in numerical integration of rate constitutive equations arising in large-deformation analysis. *International journal for numerical methods in engineering* 15, 12 (1980), 1862–1867.
- [37] HWU, Y.-J., AND LENARD, J. A finite element study of flat rolling. *Journal of Engineering Materials and Technology* 110, 1 (1988), 22–27.
- [38] JOHNSON, K. L., AND JOHNSON, K. L. *Contact mechanics*. Cambridge university press, 1987.
- [39] JUNG, D. Study of dynamic explicit analysis in sheet metal forming processes using faster punch velocity and mass scaling scheme. *Journal of materials engineering and performance* 7, 4 (1998), 479–490.
- [40] KOBAYASHI, S., AND LI, G. Rigid-plastic finite-element analysis of plane strain rolling. *Journal of Engineering for Industry* 104 (1982), 55.
- [41] KOBAYASHI, S., OH, S.-I., AND ALTAN, T. *Metal forming and the finite-element method*. Oxford university press, 1989.
- [42] KRÖNER, E. Allgemeine kontinuumstheorie der versetzungen und eigenspannungen. *Archive for Rational Mechanics and Analysis* 4, 1 (1959), 273–334.
- [43] LEE, E. H. Elastic-plastic deformation at finite strains. *Journal of applied mechanics* 36, 1 (1969), 1–6.
- [44] LEE, J. D. A large-strain elastic-plastic finite element analysis of rolling process. *Computer methods in applied mechanics and engineering* 161, 3 (1998), 315–347.
- [45] LENARD, J., AND PIETRZYK, M. Rolling process modelling. In *Numerical Modelling of Material Deformation Processes*, P. Hartley, I. Pillinger, and C. Sturgess, Eds. Springer London, 1992, pp. 274–302.
- [46] LENARD, J. G. *Primer on flat rolling*. Newnes, 2013.
- [47] LEONOV, A. I. On the conditions of potentiality in finite elasticity and hypo-elasticity. *International Journal of Solids and Structures* 37, 18 (2000), 2565–2576.
- [48] LI, Y.-F., AND NEMAT-NASSER, S. An explicit integration scheme for finite-deformation plasticity in finite-element methods. *Finite elements in analysis and design* 15, 1 (1993), 93–102.
- [49] LIU, C., HARTLEY, P., STURGESS, C., AND ROWE, G. Elastic-plastic finite-element modelling of cold rolling of strip. *International journal of mechanical sciences* 27, 7 (1985), 531–541.
- [50] MAIRE, P.-H., ABGRALL, R., BREIL, J., LOUBÈRE, R., AND REBOURCET, B. A nominally second-order cell-centered lagrangian scheme for simulating elastic-plastic flows on two-dimensional unstructured grids. *Journal of Computational Physics* 235 (2013), 626–665.

- [51] MALEKI, H., BAGHERZADEH, S., MOLLAEI-DARIANI, B., AND ABRINIA, K. Analysis of bonding behavior and critical reduction of two-layer strips in clad cold rolling process. *Journal of Materials Engineering and Performance* 22, 4 (2013), 917–925.
- [52] MANIATTY, A., DAWSON, P., AND WEBER, G. An eulerian elasto-viscoplastic formulation for steady-state forming processes. *International journal of mechanical sciences* 33, 5 (1991), 361–377.
- [53] MARUSICH, T., AND ORTIZ, M. Modelling and simulation of high-speed machining. *International Journal for Numerical Methods in Engineering* 38, 21 (1995), 3675–3694.
- [54] MATSUOKA, S.-I. Effects of cold-rolling on the cold forging of solid polymer. *Journal of Materials Processing Technology* 84, 1 (1998), 175–180.
- [55] MCGLAMERY, R. M. Cold rolling film of high density ethylene polymer, Apr. 2 1963. US Patent 3,083,410.
- [56] MCMEEKING, R. M., AND RICE, J. Finite-element formulations for problems of large elastic-plastic deformation. *International Journal of Solids and Structures* 11, 5 (1975), 601–616.
- [57] MONTELLA, G., GOVINDJEE, S., AND NEFF, P. The exponentiated hencky strain energy in modeling tire derived material for moderately large deformations. *Journal of Engineering Materials and Technology* 138, 3 (2016), 031008.
- [58] MORI, K., OSAKADA, K., AND ODA, T. Simulation of plane-strain rolling by the rigid-plastic finite element method. *International Journal of Mechanical Sciences* 24, 9 (1982), 519–527.
- [59] MOURAD, H. M., BRONKHORST, C. A., ADDESSIO, F. L., CADY, C. M., BROWN, D. W., CHEN, S. R., AND GRAY, G. T. Incrementally objective implicit integration of hypoelastic-viscoplastic constitutive equations based on the mechanical threshold strength model. *Computational Mechanics* 53, 5 (2014), 941–955.
- [60] MOVAHEDI, M., MADAAH-HOSSEINI, H., AND KOKABI, A. The influence of roll bonding parameters on the bond strength of al-3003/zr soldering sheets. *Materials Science and Engineering: A* 487, 1 (2008), 417–423.
- [61] MUKERJEE, K. K. *A critical review of the mechanics of metal rolling, its application to the design of hot strip mills; a major technical report*. PhD thesis, Concordia University, 1973.
- [62] MULLIKEN, A., AND BOYCE, M. Mechanics of the rate-dependent elastic-plastic deformation of glassy polymers from low to high strain rates. *International journal of solids and structures* 43, 5 (2006), 1331–1356.
- [63] MUÑIZ, A. R. *Non-linear finite element method simulation and modeling of the cold and hot rolling processes*. PhD thesis, Virginia Polytechnic Institute and State University, 2007.
- [64] NADAI, A. The forces required for rolling steel strip under tension. *J. appl. Mech* 6 (1939), A54–62.

- [65] NAGTEGAAL, J. C., PARKS, D. M., AND RICE, J. On numerically accurate finite element solutions in the fully plastic range. *Computer methods in applied mechanics and engineering* 4, 2 (1974), 153–177.
- [66] NEFF, P., LANKEIT, J., GHIBA, I.-D., MARTIN, R., AND STEIGMANN, D. The exponentiated hencky-logarithmic strain energy. part ii: Coercivity, planar polyconvexity and existence of minimizers. *Zeitschrift für angewandte Mathematik und Physik* 66, 4 (2015), 1671–1693.
- [67] NEMAT-NASSER, S., AND LI, Y.-F. A new explicit algorithm for finite-deformation elastoplasticity and elastoviscoplasticity: performance evaluation. *Computers & structures* 44, 5 (1992), 937–963.
- [68] OH, S., AND KOBAYASHI, S. An approximate method for a three-dimensional analysis of rolling. *International Journal of Mechanical Sciences* 17, 4 (1975), 293–305.
- [69] OROWAN, E. The calculation of roll pressure in hot and cold flat rolling. *Proceedings of the Institution of Mechanical Engineers* 150, 1 (1943), 140–167.
- [70] PADHYE, N. *Sub- T_g , solid state, plasticity-induced bonding of polymeric films and continuous forming*. PhD thesis, Massachusetts Institute of Technology, Cambridge, MA, USA, 2015.
- [71] PADHYE, N. *Molecular Mobility in Deforming Polymer Glasses: Theories and Applications*. Springer Nature, 2021.
- [72] PADHYE, N., PARKS, D. M., SLOCUM, A. H., AND TROUT, B. L. A roll-bonding machine for polymeric films. In *American Society for Precision Engineering, 2014 Annual Meeting* (2014), vol. 59, pp. 357–360.
- [73] PADHYE, N., PARKS, D. M., TROUT, B. L., AND SLOCUM, A. H. A new phenomenon: Sub- t_g , solid-state, plasticity-induced bonding in polymers. *Scientific Reports* 7 (2017).
- [74] PADHYE, N., AND VALLABH, A. Deformation-induced bonding of polymer films below the glass transition temperature. *Journal of Applied Polymer Science* 138, 41 (2021), 50934.
- [75] PADHYE, N., AND VALLABH, A. Dilatational-plasticity opens a new mechanistic pathway for macromolecular transport across polymeric interfaces yielding solid-state bonding. *arXiv preprint arXiv:2205.04015* (2022).
- [76] PASLAY, P. R. *Calendering of an elastic-viscous material*. PhD thesis, Massachusetts Institute of Technology, 1955.
- [77] PHUA, Y., CHOW, W., AND MOHD ISHAK, Z. Mechanical properties and structure development in poly (butylene succinate)/organo-montmorillonite nanocomposites under uniaxial cold rolling. *Express Polymer Letters* 5, 2 (2011), 93–103.
- [78] PINSKY, P. M., ORTIZ, M., AND PISTER, K. S. Numerical integration of rate constitutive equations in finite deformation analysis. *Computer Methods in Applied Mechanics and Engineering* 40, 2 (1983), 137–158.

- [79] PRIOR, A. Applications of implicit and explicit finite element techniques to metal forming. *Journal of Materials Processing Technology* 45, 1-4 (1994), 649–656.
- [80] RASHID, M. Incremental kinematics for finite element applications. *International journal for numerical methods in engineering* 36, 23 (1993), 3937–3956.
- [81] ROBERTS, W. L. *Cold rolling of steel*. Dekker, 1978.
- [82] ROBERTS, W. L. *Hot rolling of steel*. CRC Press, 1983.
- [83] ROWE, G. W., STURGESS, C., AND HARTLEY, P. *Finite-element plasticity and metalforming analysis*. Cambridge university press, 2005.
- [84] ROWE, G.W., S. C. H. P., AND PILLINGER, I. *Finite-Element Plasticity and Metalforming Analysis*. Oxford university press, 1991.
- [85] RYCKMAN, R. A., AND LEW, A. J. An explicit asynchronous contact algorithm for elastic body–rigid wall interaction. *International Journal for Numerical Methods in Engineering* 89, 7 (2012), 869–896.
- [86] SIEBEL, E. Berichte des walzwerksausschusses. *Verein deutscher Eisenhüttenleute* 37 (1924).
- [87] SIEBEL, E. Werkstoffausschuss. *Stahl und Eisen* 71 (1925).
- [88] SIMO, J. C. Numerical analysis and simulation of plasticity. *Handbook of numerical analysis* 6 (1998), 183–499.
- [89] SIMO, J. C., AND PISTER, K. S. Remarks on rate constitutive equations for finite deformation problems: computational implications. *Computer Methods in Applied Mechanics and Engineering* 46, 2 (1984), 201–215.
- [90] SMITH, C., SCOTT, F., AND SYLWESTROWICZ, W. Pressure distribution between stock and rolls in hot and cold flat rolling. *JOURNAL OF THE IRON AND STEEL INSTITUTE* 170, 4 (1952), 347–359.
- [91] TIEU, A., AND LIU, Y. Friction variation in the cold-rolling process. *Tribology International* 37, 2 (2004), 177–183.
- [92] TROUT, B. L., HATTON, T. A., CHANG, E., EVANS, J. M., MASCIA, S., KIM, W., SLAUGHTER, R. R., DU, Y., DHAMANKAR, H. H., FORWARD, K. M., ET AL. Layer processing for pharmaceuticals, Dec. 8 2015. US Patent 9,205,089.
- [93] TSELIKOV, A. The influence of external friction and tension on roll face pressure. *Metallurgiya* 6 (1939), 61–76.
- [94] VON KÁRMÁN, T. On the theory of rolling. *Z. Angew. Math. Mech* 5 (1925), 130–141.
- [95] WANG, L., AND ATLURI, S. An analysis of an explicit algorithm and the radial return algorithm, and a proposed modification, in finite plasticity. *Computational mechanics* 13, 5 (1994), 380–389.

- [96] WEBER, G. G., LUSH, A., ZAVALIANGOS, A., AND ANAND, L. An objective time-integration procedure for isotropic rate-independent and rate-dependent elastic-plastic constitutive equations. *International journal of plasticity* 6, 6 (1990), 701–744.
- [97] WUSATOWSKI, Z. *Fundamentals of rolling*. Elsevier, 2013.
- [98] ZHANG, W., AND BAY, N. A numerical model for cold welding of metals. *CIRP Annals-Manufacturing Technology* 45, 1 (1996), 215–220.
- [99] ZIENKIEWICZ, O., AND GODBOLE, P. Flow of plastic and visco-plastic solids with special reference to extrusion and forming processes. *International Journal for Numerical Methods in Engineering* 8, 1 (1974), 1–16.
- [100] ZIENKIEWICZ, O., JAIN, P., AND ONATE, E. Flow of solids during forming and extrusion: some aspects of numerical solutions. *International Journal of Solids and Structures* 14, 1 (1978), 15–38.
- [101] ZIENKIEWICZ, O., TAYLOR, R., AND TOO, J. Reduced integration technique in general analysis of plates and shells. *International Journal for Numerical Methods in Engineering* 3, 2 (1971), 275–290.